Ocean Engineering 222 (2021) 108360

Contents lists available at ScienceDirect

Ocean Engineering

journal homepage: www.elsevier.com/locate/oceaneng

Validation of the dynamic load characteristics on a Tidal Stream Turbine when subjected to wave and current interaction

Catherine Lloyd[a,*], Matthew Allmark[a], Stephanie Ordonez-Sanchez[b], Rodrigo Martinez[b], Cameron Johnstone[b], Gregory Germain[c], Benoit Gaurier[c], Allan Mason-Jones[a], Tim O'Doherty[a]

[a] Cardiff Marine Energy Research Group, School of Engineering, Cardiff University, Queens Buildings, 14-17, The Parade, Cardiff, CF24 3AA, UK
[b] Energy Systems Research Unit, Department of Mechanical and Aerospace Engineering, University of Strathclyde, 75 Montrose Street, Glasgow, G1 1XQ, UK
[c] IFREMER, Marine and Structures Laboratory, Centre Manche, Mer du Nord, 150 Quai Gambetta, 62200, Boulogne-sur-Mer, France

ARTICLE INFO

Keywords:
Tidal stream turbine
Wave-current interaction
Computational fluid dynamics
Regular waves
Experimental validation
Marine energy

ABSTRACT

A comparison of a tidal turbine's performance and structural loads is conducted using lab-scale numerical models and experimental testing under multiple current-only and wave-current conditions at the IFREMER wave-current flume. Experimental testing, used to validate CFD models, was accomplished using a 0.9 m diameter, 3-bladed tidal turbine and had a blockage ratio of 8% while the turbine was submerged. Initial investigations analysed the performance and loads on the turbine under uniform and profiled current-only conditions. The presence of a profiled velocity gradient was found to have a negligible effect on the average performance characteristics; however, transient thrust, torque and out of plane bending moment loads experienced much greater variations. These load fluctuations were further increased with increasing levels of shear in the velocity profile, while peaks in the turbine loads coincided with its rotational frequency. The addition of regular, Stokes 2nd Order Theory waves added to the complexity of the flow conditions experienced by the turbine. The effect on the average performance characteristics were negligible while the total turbine thrust and torque fluctuations increased by 35 times that of the current-only cases. Peaks in the loads aligned with the wave surface elevation, indicating the importance of transient analyses of dynamic loads.

1. Introduction

World energy consumption is predicted to increase by 28% from 2015 to 2040 (U.S Energy Information Administration, 2017). However, it is unsustainable and undesirable to generate electricity from fossil fuels, particularly due to global concerns about climate change and global warming which are a direct result of increasing concentrations of Green House Gases (GHG) from burning fossil fuels. The European Commission (EC) has set targets to reduce GHG emissions progressively and commit to net zero by 2050 (European Commission, 2020a). The current framework sets out to reduce GHG emissions by 40%, improve energy efficiency by 32.5%, and to secure 32% of Europe's energy from renewable sources by 2030 (European Commission, 2020b).

The oceans cover around 70% of the earth's surface and is therefore an extensive and highly predictable renewable energy source which is yet to be fully utilised. Europe is reported to hold 20–30% of the global tidal resource, of which 80% is located in and around the coastlines of the UK and France. If fully exploited using current technology, wave and tidal power could supply at least 10% of the UK's electricity (Renewable Energy Association, 2019). This could go some way to help achieve GHG emissions targets, replace the imminent depletion of energy supply through nuclear outputs (UK Department for Business Energy and Industrial Strategy, 2020), and create a diverse energy mix for a sustainable future.

The advancement of Horizontal Axis Tidal Turbines (HATTs) mean that over 75% of companies are developing full-scaled HATT devices over other Tidal Stream Turbine (TST) devices (European Commission, 2017; Ocean Energy Europe, 2018). A significant problem for tidal stream energy developers is the spatio-temporal complexity in the flow which makes deployment and device survivability a challenge (Chen and Lam, 2015; Togneri and Masters, 2016). To enable HATT devices to become commercially viable, device components must be able to withstand substantial spatial, and temporal, sub-surface forces generated by

---

* Corresponding author.
E-mail address: LloydC11@cardiff.ac.uk (C. Lloyd).

https://doi.org/10.1016/j.oceaneng.2020.108360
Received 11 August 2020; Received in revised form 3 November 2020; Accepted 4 November 2020

Nomenclature

a	Wave amplitude $[m]$
A_t	Swept area of turbine $[m^2]$
BM_x	Out of plane bending moment $[Nm]$
c	Chord length $[m]$
C	Wave celerity $[m/s]$
C_p	Power coefficient [-] $\left(\frac{Q\omega}{\frac{1}{2}\rho A_t \overline{W}_{vol}^{\,3}}\right)$
C_q	Torque coefficient [-] $\left(\frac{Q}{\frac{1}{2}\rho A_t \overline{W}_{vol}^{\,2} R}\right)$
C_t	Thrust coefficient [-] $\frac{T}{\frac{1}{2}\rho A_t \overline{W}_{vol}^{\,2}}$
h	Water depth $[m]$
H	Wave height $[m]$
k	Wave number $[rad/m]$
L	Wavelength $[m]$
Q	Torque $[Nm]$
R	Turbine radius $[m]$
Re	Reynolds number [-]
t	Time $[s]$
Δt	Time step $[s]$
T	Thrust $[N]$
T_a	Apparent wave period, stationary ref. frame $[s]$
T_r	Relative wave period, moving ref. frame $[s]$
v_a	Vertical velocity component under a wave, stationary ref. frame $[m/s]$
w_a	Horizontal velocity component under a wave, stationary ref. frame $[m/s]$
w_r	Horizontal velocity component under a wave, moving ref. frame $[m/s]$
$w^{'}$	Velocity fluctuation $[m/s]$
$\overline{W}$	Average streamwise velocity $[m/s]$
$\overline{W}_{vol}$	Volumetrically averaged streamwise velocity $[m/s]$
η	Wave surface elevation $[m]$
θ	Angle $[^\circ]$
λ	Tip speed ratio [-]
ρ	Density $[kg/m^3]$
$\varnothing$	Diameter $[m]$
ω	Angular velocity of the turbine $[rad/s]$

tidal currents, surface waves and turbulence, to minimise device downtime as well as operation and maintenance costs, thus help reduce the cost of electricity generation.

Lab-scale experiments can be conducted to reproduce realistic ocean conditions and to quantify the magnitude of these sub-surface forces prior to the full-scale design, manufacture and testing of a device. TSTs have been widely characterised under uniform current conditions (Allmark et al., 2018; Bahaj et al., 2007; Gaurier et al., 2015; Maganga et al., 2010), however, it is important to understand the impact of additional loadings induced by profiled current conditions as well as surface waves which create oscillatory motions, penetrating the water column by up to half the wavelength (Sorensen, 2006). The ocean environment will never experience a regular wave field, yet regular waves of relevant heights and wave periods can be used to quantify the extreme loadings experienced by the TST components (Holst et al., 2015). Previous studies, (Barltrop et al., 2007; Galloway et al., 2010; Gaurier et al., 2020a, 2020b; Henriques et al., 2014; Lust et al., 2013; Luznik et al., 2013; Martinez et al., 2020; Ordonez-Sanchez et al., 2016; Porter et al., 2020; Sos et al., 2017), have investigated the performance of a TST under regular wave conditions and found that the average performance characteristics were very similar to tests conducted under current-only conditions. However, oscillatory motions induced by waves presented significant cyclic variations, responsible for fluctuations in the thrust and torque loadings in excess of 35% of the mean rotor load (Galloway et al., 2010; Ordonez-Sanchez et al., 2019). This can lead to extreme loadings on the drivetrain and accelerated fatigue of the individual turbine components.

With advances in computational processing times and the accessibility of software, Computational Fluid Dynamics (CFD) has become a widely adopted tool to develop numerical simulations to characterise the performance and loadings of marine devices in various flow conditions. Numerical models still require validation, however, the number of experiments needed is less than required for a full experimental test campaign. Steady state analyses can be used to model time-independent flows, however, analyses which account for transient flow features provide results of a higher resolution than steady state models (ANSYS CFX Modelling Guide; Hafeez et al., 2019). Transient simulations are necessary to examine cyclic loadings induced by complex flow features, although at a much greater computational expense than steady state simulations. Transient CFD models have been used to characterise TST devices (Bai et al., 2014; Li et al., 2019; McSherry et al., 2011; O'Doherty et al., 2009; Sun et al., 2008; Yan et al., 2017), investigate profiled current flows (Hafeez et al., 2019; Mason-Jones, 2010; Mason-Jones et al., 2013; O'Doherty et al., 2010), and examine different methods of wave propagation (Bihs et al., 2016; Finnegan and Goggins, 2012; Jacobsen et al., 2012; Lal and Elangovan, 2008; Lambert, 2012; Liang et al., 2010; Lloyd et al., 2019b; Marques Machado et al., 2018; Tian et al., 2018). However, few studies have investigated the combined effects of a profiled velocity gradient, waves, and turbine interaction. A study by Tatum et al. (2016) analysed the individual turbine component loadings induced by a uniform current velocity and surface waves, finding that wave action had a significant effect on the fluctuation of the thrust and power, as well as the shaft bending moment. Interaction with a velocity profile was also investigated and found that the addition of a profiled velocity gradient had a significant effect on the bending moment of the turbine blades. Investigating the significance of individual blade loadings experimentally, requires the use of fully instrumented model TSTs which is expensive and difficult to achieve in controlled test scenarios. Numerical modelling can therefore provide a cheaper and alternative method to quantify these complex loadings which are crucial for developers needing to make informed decisions about the turbine rotor and blade design, prior to their manufacture.

The focus of this study is to examine the impact that complex flow conditions, such as profiled velocity gradients or surface waves, can have on the individual turbine component loadings and performance of a HATT. The research methods used include experimental lab-scale testing at the French Research Institute for Exploitation of the Sea (IFREMER) wave-current flume as well as the use of numerical CFD modelling using ANSYS CFX software. This paper presents the methodology used to develop a free surface, multiphase model capable of simulating turbine rotation in uniform and profiled current flows, as well as in regular wave fields. All numerical models are initially validated using lab-scale experimental data allowing further investigation into the transient turbine loadings which were unattainable through the experimental test campaign. This study presents the turbine performance under uniform and profiled current-only conditions, as well as under wave-current conditions using Stokes 2nd Order Theory (S2OT) regular waves which are superimposed upon the profiled current velocities. Comparisons are made between the numerical CFD models developed, and experimental data obtained by Cardiff and Strathclyde

Universities at the IFREMER wave-current flume.

2. Experimental testing

2.1. Model scale turbine

A 1:20 scale HATT was designed and manufactured by the Cardiff Marine Energy Research Group (CMERG) (Mason-Jones, 2010), as shown in Fig. 1A. The blade design was based upon the Wortmann FX63-137 aerofoil, as shown in Fig. 1B, while the optimum settings for this design are summarised in Table 1. A full description of the blade and turbine design and manufacture are detailed by (Allmark et al., 2020) and (Ellis et al., 2018), respectively.

In order to quantify the dynamic loadings on the turbine under various flow conditions, the turbine was fully instrumented. The rotor thrust/torque transducers and the out of plane bending moment transducers for each turbine blade had a sample rate of 200 Hz and were calibrated as detailed in (Lloyd, 2020). A Haidenhain optical encoder was used to measure the turbine position with a sample rate of 45 Hz, and moisture sensors were installed to detect for leakages. A full uncertainty analysis of the measured variables used in the experimental testing can be found in (Allmark et al., 2020; Lloyd, 2020), with a summary presented in Table 2.

2.2. Experimental set up

Experimental testing of the model scale HATT was carried out at the IFREMER wave-current flume, Boulogne-Sur-Mer, France (Gaurier et al., 2018). The flume dimensions are 4 m wide, 2 m deep and 18 m long, as shown in Fig. 2, with a general flow turbulence of ≈3% (Gaurier et al., 2013). The flume has the capability to produce streamwise flow velocities between 0.1 and 2.2 m/s, with and without waves. Regular wave generation, between $f = 0.5$-2 Hz, is achieved using 8 displacement paddles which span the full 4 m width of the flume and, when fully submerged, sit 0.5 m into the water column. A physical beach was located at the opposite end of the flume to the wave maker to dampen the waves and prevent reflection from the end of the tank.

For all experimental testing, the turbine was installed 4 m downstream from the wave maker at a depth of 1 m and centralised in the cross-stream direction. This gave a clearance of 0.61∅ (27% of the water depth) between the turbine, positioned at Top Dead Centre (TDC), and the water surface in still water conditions. There was a blockage ratio of 8% while the turbine was submerged in the IFREMER wave-current flume. This ratio was low enough not to interfere with the flow characteristics (Howell et al., 2009), though for direct comparison the CFD models reflected the flume boundary conditions, as discussed in Section 3. A 0.09 m stanchion supported the turbine and held it stationary within the flume. The pitch angle for each turbine blade was set to 6° ± 0.5°. Experimental tests were carried out with speed control at a number of angular velocities in order to generate performance characteristics over a range of Tip Speed Ratios (TSRs) (λ) (0–7) based on the average streamwise water velocity ($\overline{W}$), as shown by Equation (1).

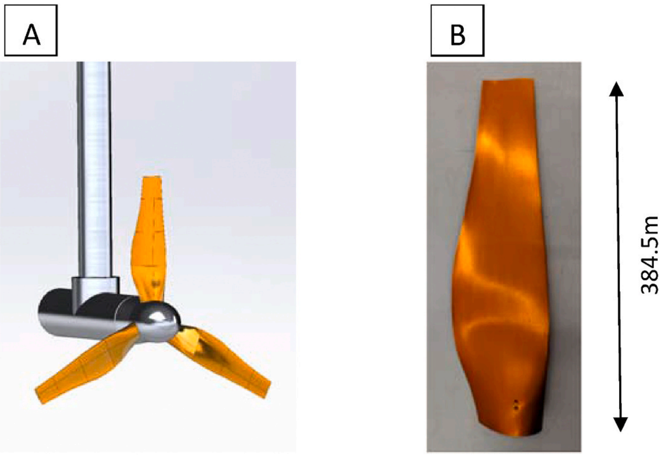

Fig. 1. Diagram of: A) the full turbine and; B) the new blade design.

Table 1
Main turbine characteristics summary.

Characteristic	Description
No. Blades	3
Blade length	384.5 mm
Pitch angle	6.24°
Twist distribution	19°
Turbine diameter	900 mm
Hub diameter	130 mm

Table 2
Summary of uncertainties for turbine instrumentation.

Characteristic	μ_{tot} as a % of mean value (%)
Thrust transducer, T (Nm)	3.06
Torque transducer, Q (Nm)	3.91
Out of plane bending moment, BM_x (Nm)	2.54
Angular velocity, ω (rad/s)	0.31
Turbine radius, R (m)	1.11

$$\lambda = \frac{\omega R}{\overline{W}} \tag{1}$$

A Dantec 2D Laser Doppler Anemometry (LDA) was used to measure the instantaneous flow velocities in the streamwise and vertical directions with a sample rate of 200 Hz. The measurement volume was initially aligned 1 m upstream of the centre of the turbine nose cone. It was then moved to measure the flow velocity at multiple locations through the water column at depths of −0.55, −0.68, −0.81, −0.94, −1, −1.13, −1.26, −1.39 and −1.52 m from the SWL for the uniform current cases, and every 0.2 m between −0.4 m and −1.6 m from the SWL for the profiled current cases. This covered the full diameter of the turbine which occupied a water depth between −0.55 m and −1.45 m from the SWL. Fig. 3 shows the setup of the turbine and the measurement equipment at the IFREMER wave-current flume. A Churchill controls capacitance type wave probe was used to track the water surface elevation with a sample rate of 100 Hz. An uncertainty analysis for the flow measurement devices is detailed in (Lloyd, 2020).

2.3. Experimental procedure

2.3.1. Current-only cases

Current-only experiments were carried out with both uniform and profiled flows. For all test cases, a target streamwise velocity of 1.0 m/s was used which equated to a chord based Reynolds number of $Re_{0.7chord} = 6.48\,x\,10^4$ (Allmark et al., 2020), as defined by Equation (2), where $c_{0.7}$ is the chord length at 70% of the turbine radius. Previous experimental testing confirmed that Reynolds effects become negligible, with a variation <1%, for Reynold's numbers above $Re_{0.7chord} = 6.48\,x\,10^4$ (Allmark et al., 2020).

$$Re_{0.7chord} = \frac{\rho c_{0.7} W}{\mu} \tag{2}$$

Flow straighteners placed in the upstream area of the flume aided the generation of uniform flow conditions (U) while the wave maker paddles were fully removed (NOWM). Profiled flow conditions could be generated by positioning the wave maker paddles in the upper section of the water column to create a blockage. The wave maker could be positioned

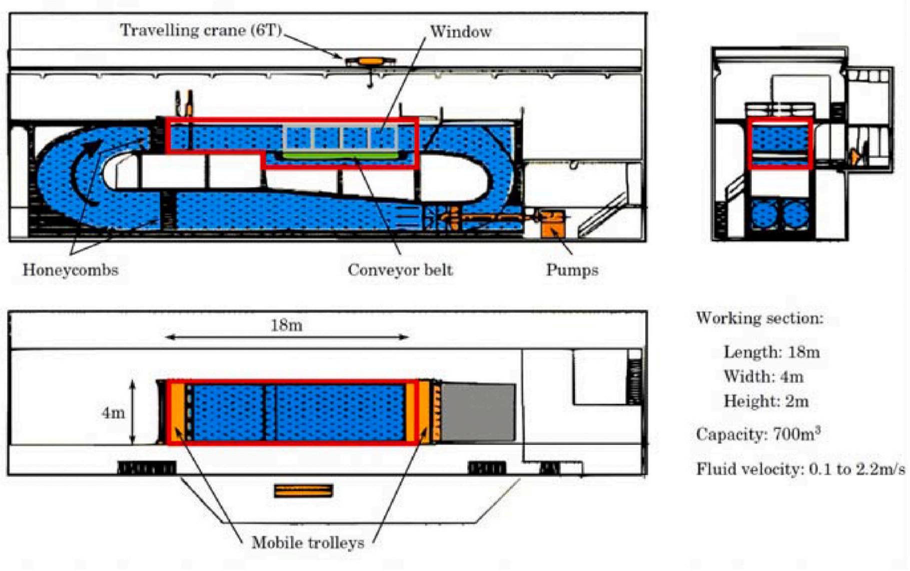

Fig. 2. IFREMER flume tank schematic, figure reproduced from (Gaurier et al., 2013).

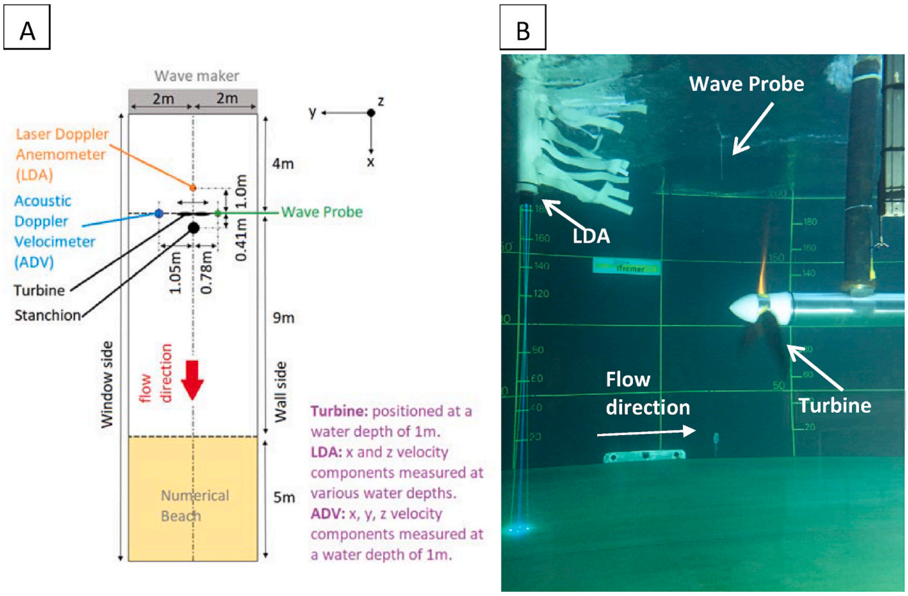

Fig. 3. A plan view of the IFREMER experimental setup of flow measurement equipment and the turbine positioning, (A) diagrammatically, and (B) a picture from the facility.

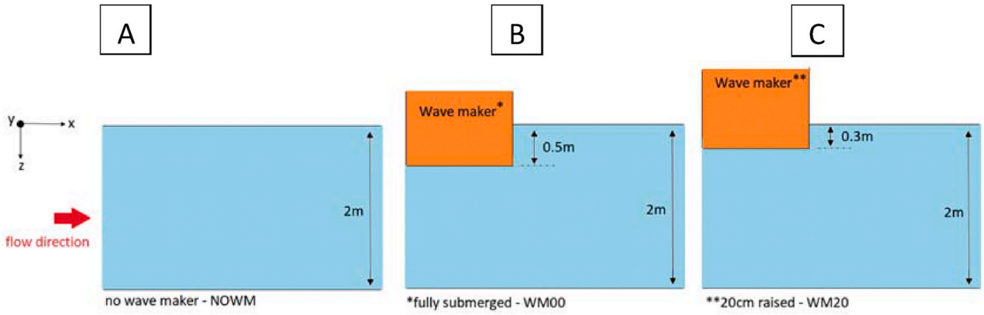

Fig. 4. IFREMER experimental setup of wave maker when at position: A) NOWM (no wave maker), B) WM00 (fully submerged) and; C) WM20 (raised by 20 cm).

in two different locations, WM00 or WM20, creating two different velocity profiles, Profile 1 (P1) and Profile 2 (P2), respectively. WM00 and WM20 refer to the wave maker being either fully submerged (to a depth of 50cm/raised by 0 cm) or partially submerged (to a depth of 30cm/raised by 20 cm) in the top of the water column, respectively. For all current-only cases the wave maker was not operational even though it was used to induce the differing velocity profiles. Each of the flow scenarios are depicted in Fig. 4 and summarised in Table 3.

2.3.2. Wave-current cases

Two different regular waves were used to investigate the effect of combined wave-current conditions on the performance and loadings of the model scale TST. Both waves were intermediate, S2OT waves and were superimposed upon the profiled current velocity produced by the wave maker position. Wave 1 (W1) was superimposed upon P1, and Wave 2 (W2) upon P2. These waves were tested in a water depth (h) of 2 m but would be representative of tidal sites with a water depth of between 25 and 40 m by scaling the wave characteristics to match the relative depth and wave steepness criteria. This would result in a wave height (H), wave period (T_r) and wavelength (L) as described by W1S and W2S, as shown in Table 4.

Five different types of flow condition were tested, three current-only (U, P1, P2) and two wave-current cases (P1W1, P2W2), as outlined in Tables 3 and 4. The turbine was operated at a range of angular velocities to generate a full set of performance curves for the power coefficient (C_p), thrust coefficient (C_t) and torque coefficient (C_q), as defined in the Nomenclature. The flume and TST were brought up to speed before data capture commenced, recording flow and turbine measurements for between 100 and 200 s.

3. Numerical methodology

CFD was used to create numerical models to replicate the testing carried out experimentally at the IFREMER flume. This enabled a direct comparison between the numerical and experimental results, eliminating the need for any blockage correction errors. ANSYS ICEM 18.0 (ANSYS Inc, n.d.) was used to create the geometry and mesh while ANSYS CFX 18.0 (ANSYS Inc, n.d.) was used for the physics setup of the model and the solver. The model development has been split up into the following sections: 3.1 Domain geometry and mesh characteristics, 3.2 Model setup and 3.3 Current flow and wave generation.

3.1. Domain geometry and mesh characteristics

Fig. 5 shows an overview of the model geometry which was individually optimised dependent on the flow conditions and experimental facility dimensions (Lloyd et al., 2019b). The model domain was split up into a main fluid domain and a rotating subdomain which enclosed the turbine. A free surface model was developed to allow 2-phase multiphase flow where both water and air phases are present. The free surface interface was located at a water depth of 2 m which is 70% of the overall domain height (2.86 m), leaving the remaining upper section of the domain as air (Lloyd et al., 2019b). The width of the domain was the same as the IFREMER flume (4 m), to ensure the blockage ratio of the turbine was the same between experimental and numerical testing. The domain length was varied based on requirements for each individual simulation. For current-only conditions, a domain length of 20 m was used, allowing for adequate wake development while being suitably long that the domain outlet does not interfere with the turbine characteristics (Ebdon, 2019; Ellis et al., 2018; Mason-Jones, 2010). For wave-current simulations, the length of the domain was varied depending on the simulated wave characteristic wavelength, as shown in Fig. 6. The domain length was found to be optimal when set to allow the propagation of 8–10 waves (Lloyd et al., 2019b) before reaching the end of the domain. A numerical beach of twice the wavelength ($2L$) was incorporated to prevent any reflection of the waves from the end of the domain which corresponded to a main domain length of 80 m and 50 m for simulations using W1 and W2, respectively. This was imposed by applying a general momentum source acting in the direction of wave propagation, which was used to force the velocity in this region to be the same as the current velocity, removing the oscillatory effects of the wave (Lloyd, 2020).

Table 3
Summary of current characteristics and wave maker settings.

Current Name	Current Profile	Target $\overline{W}$over swept area (m/s)	Wave maker position	Distance wave maker is submerged in water column (cm)	Distance wave maker is raised from fully submerged position (cm)
U	Uniform	1.0	NOWM	–	–
P1	Profiled	1.0	WM00	50	0
P2	Profiled	1.0	WM20	30	20

A cylindrical rotating subdomain was created to enclose the turbine blades and hub, as shown in Fig. 5. This allowed the Multiple Frames of Reference (MFR) technique (ANSYS CFX Theory Guide) to be used allowing the turbine subdomain to rotate around the z-axis at a set angular velocity, simulating the turbine rotation. The ‘transient rotor stator’ interface model was used to account for the transient interaction effects at the sliding interface between these two domains. The cylinder was 1.3 m in diameter and 0.4 m wide, as recommended by (Ellis et al., 2018), as it was found that a smaller diameter would influence the turbine results yet a bigger diameter had no effect. Table 5 provides a summary of the dimensions used for each numerical model.

The mesh for the main fluid domain was generated using a ‘top down’ blocking strategy to create a structured, HEXA mesh (ANSYS CFX Modelling Guide). HEXA meshing is highly space efficient and is advantageous in comparison to an unstructured TETRA mesh as it requires less computational points, having a higher spatial resolution, and better aspect ratio, all of which increase the resolution of the simulation (Raval, 2008). Specifically, for wave modelling, it is important to have a region of increased mesh resolution around the air-water interface spanning the entire wave height to maintain the desired surface resolution at all points along the wavelength. Optimum mesh sizing around the free surface used 10 cells over the wave height and 120 cells per wavelength (Lloyd et al., 2019b), as shown in Fig. 7. Table 6 presents the mesh sizing parameters for the main fluid domain in each simulation.

The mesh around the turbine was achieved using a ‘bottom up’ meshing method, creating a surface mesh which was refined to produce a finer volume mesh, establishing a TETRA mesh. Inflation layers were added to the surface of the turbine to increase the boundary layer resolution perpendicular to the surface. Table 7 shows the turbine subdomain optimum mesh sizing parameters, based on a mesh study conducted by (Lloyd et al., 2019a).

The main fluid domain and turbine subdomain meshes were combined to create an overall mesh suitable for simulating S2OT waves, uniform and profiled current flows, as well as measuring turbine performance and loading characteristics. Fig. 7 shows an example of the final mesh used to simulate wave-current and turbine interaction using the characteristics of P2W2. The maximum aspect ratio for all mesh components is well within the recommendation of <1000 ((ANSYS Inc, n.d.). The number of elements in the final meshes are between 7.4 and 15.5 million depending on the flow characteristics used in the simulation. Further information about the mesh studies undertaken and types of mesh used can be found in (Lloyd, 2020).

3.2. Model setup

ANSYS CFX 18.0 (ANSYS Inc, n.d.) was used to define the physics of the model and to enable the numerical simulation to be solved. A homogenous, air-water multiphase model was used to simulate free surface

Table 4
Summary of wave characteristics.

Wave Name	Water Depth,h (m)	Wave maker position	H(m)	T_r(s)	L(m)	Steepness H/L	Relative Depth h/L	Depth Condition
W1	2	WM00	0.09	2.566	9.07	0.010	0.221	Intermediate
W2	2	WM20	0.11	1.917	5.61	0.021	0.357	Intermediate
W1S	25–40	–	1.1–1.8	9.0–11.5	113–181	0.010	0.221	Intermediate
W2S	25–40	–	1.5–2.4	6.8–8.6	70–112	0.021	0.357	Intermediate

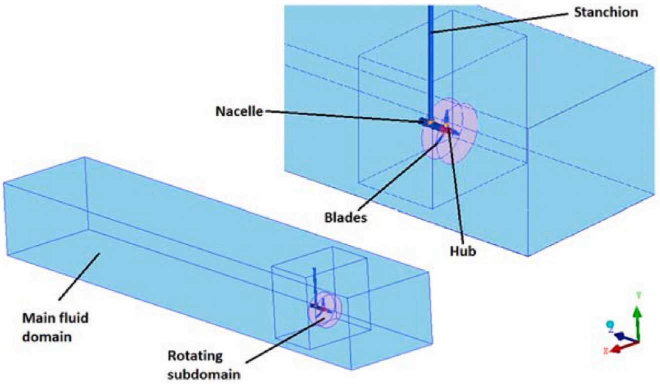

Fig. 5. Primary features in turbine numerical model.

flows. The two phases are separated by a distinct interface, using volume fractions to specify the fraction of the control volume that each fluid phase occupies (ANSYS CFX Theory Guide), and used an activated buoyancy scheme. The Shear Stress Transport (SST) statistical turbulence model (Menter, 1996) was used to close the Reynolds Averaged Navier-Stokes (RANS) equations due to its improved performance under adverse pressure gradients in comparison to the$k$-omega (k-ω) and k-epsilon (k-ε) turbulence models (ANSYS CFX Modelling Guide), as well as being proven to have no detrimental effects on the generation and propagation of regular waves (Alberello et al., 2017; Finnegan and Goggins, 2012, 2015; Lal and Elangovan, 2008). A transient analysis was carried out to capture the time dependent nature of the flow and the dynamic loading on the turbine. It was necessary to define a physical time step (Δt) to control the simulation and capture the required level of detail in the simulation as ANSYS CFX solver uses an implicit solution method (ANSYS CFX Theory Guide). The time step for current-only models incorporating a turbine (Δt_{turb}) equated to the turbine rotating by a maximum of $\theta = 5^\circ$ per time step (ANSYS CFX Reference Guide; McSherry et al., 2011), as shown by Equation (3). Therefore, the time step for each model would be varied according to the selected angular velocity. For simulations with waves, a time step (Δt_{wave}) of $T_a/50$ was found to be optimum (Lloyd, 2020), as shown by Equation (4). For combined wave-current and turbine simulations, the smaller time step of Δt_{wave} and Δt_{turb} was utilised to ensure a sufficient level of temporal resolution was achieved. Further information on setting the time step can be found in (Lloyd, 2020).

$$\Delta t_{turb} = \frac{\theta}{\omega \cdot \frac{180}{\pi}} \tag{3}$$

$$\Delta t_{wave} = T_a/50 \tag{4}$$

The boundary conditions used for the current-only and wave-current models are summarised in Table 8, while Fig. 8 shows the locations of these boundaries. The main difference between the two types of model was the use of an ‘opening’ at the inlet and outlet for simulations incorporating wave motion. This allowed bidirectional flow, into and out of the domain, which was necessary to prevent the model from crashing when simulating regular waves.

Each simulation began with a 1.0 m/s current-only flow, using a uniform or profiled velocity gradient depending on the type of simulation. If the model required wave generation, the wave characteristic was superimposed onto the current flow after 2 s of run time in order to allow the current flow to establish before the wave conditions were incorporated. Five models were generated with different combinations of current-only flow (U, P1, P2) and wave-current flow (P1W1, P2W2). The same range of TSRs (0–7) as used in the experimental testing were simulated for the uniform flow cases. However, due to the computational expense of modelling the profiled current cases and wave cases, only a single simulation for each model was executed. Previous experimental work (Allmark et al., 2020) found that the peak power of the turbine was at a TSR of 4, and therefore these complex model types used an angular velocity equivalent to a TSR of 4. Each model was set to run for 100 s with stability in each simulation reached between 40 and 70 s of run time. Monitor points were placed at a central width in the domain, 2 m upstream of the turbine at locations between $y = -0.1$ m and

Table 5
Summary of the geometry dimensions for each CFD model.

Dimensions	Current-only conditions			Wave-current conditions	
	U	P1	P2	P1W1	P2W2
Main domain, m (Length x Width x Depth)	20 x 4 x 2.86			80 x 4 x 2.86	50 x 4 x 2.86
Subdomain cylinder, m (Diameter/ Width)	1.3/0.4				
Turbine, m	0.9				

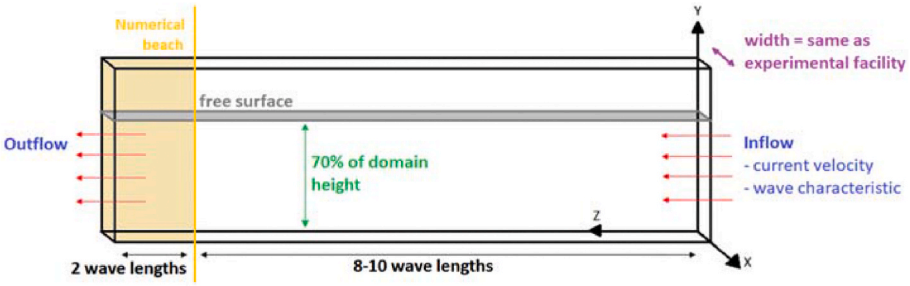

Fig. 6. General geometry setup guide for a free surface model.

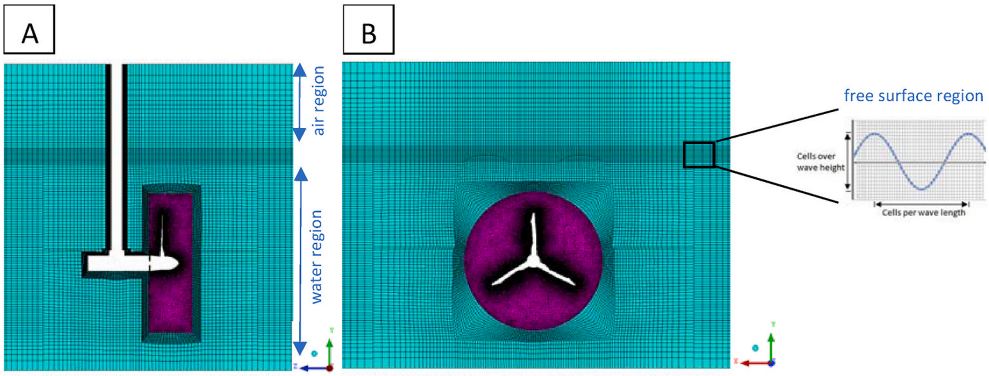

Fig. 7. An example of a final mesh for the simulation using P2W2 in the: A) YZ plane and; B) the XY plane.

Table 6
Mesh sizing parameters for the main fluid domain.

		Current-only conditions			Wave-current conditions	
		U	P1	P2	P1W1	P2W2
Region around air-water interface	Δ*y* (m)	0.01			0.01	0.01
	Δ*z* (m)	0.03			0.03	0.03
	Δ*x* (m)	0.025			0.025	0.025
Mesh expansion from interface towards the top boundary	Δ*y* (m)	0.02 → 0.1			0.02 → 0.1	0.02 → 0.1
Mesh expansion from interface towards the base boundary	Δ*y* (m)	0.01 → 0.05			0.02 → 0.03	0.02 → 0.03
Mesh expansion from centreline to side walls	Δ*x* (m)	0.02 → 0.08			0.02 → 0.12	0.02 → 0.08
Mesh expansion from inlet to outlet boundary	Δ*z* (m)	0.05 → 0.1			0.05 → 0.1	0.05 → 0.1
Total number of elements in mesh		4.3 million			12.4 million	8.8 million

$y = -1.9$ m. This enabled a visualisation of the turbine inflow conditions to be achieved over time. The torque (Q), thrust (T) and out of plane bending moment (BM_x), on the turbine blades were monitored every time step to examine the transient loadings and observe the convergence of the simulation.

All simulations were run using a High Performance Computing (HPC) cluster, ‘Hawk’, provided through access from Cardiff University. Simulations were run using between 80 and 280 processors per model. The simulations took 175–1207 h for the current-only models and 2735–4855 h for the wave-current models, dependent on the complexity of the simulation.

3.3. *Current flow and wave generation*

For uniform flow models (U), the flow characteristics were added to the inlet of the model mathematically, to reach a streamwise velocity of 1.0 m/s input using cartesian coordinates, as shown in Table 9. For models using a profiled current flow (P1 or P2), average, steady state data obtained experimentally was input to the model using a ‘Profile Method’ boundary condition at the inlet. This boundary condition used interpolated values from the flow profiles obtained during experimental testing. CFX Expression Language (CEL) expressions were then used to refer to the imported data using interpolation functions. The aim was to directly compare CFD simulations and experimental data, therefore it was important to replicate the current profile generated at the experimental facilities into the models. This method ensured minimal changes were made when transferring experimental data across to be used in

Table 8
Boundary condition details for each model type.

Boundary name	Boundary conditions	
	Current-only model	Wave-current model
inlet	velocity-inlet	velocity-inlet (opening)
outlet	pressure-outlet	pressure-outlet (opening)
top	pressure-opening	pressure-opening
base	no-slip wall	no-slip wall
walls	no-slip wall	no-slip wall
stanchion, hub, turbine blades	no-slip wall	no-slip wall

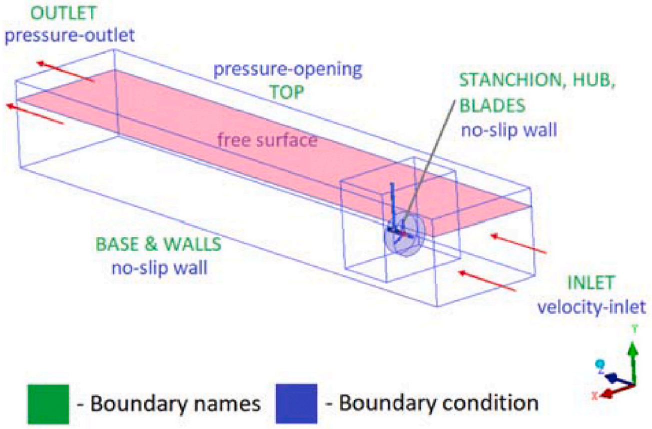

Fig. 8. Computational domain layout with boundary names and conditions imposed for the ‘free surface’ model.

Table 7
Mesh sizing parameters for the turbine subdomain.

Element size on each part (m)					Inflation layer properties			Total elements (millions)
MFR cylinder	Blade tip	Blade middle	Blade root	Hub	First layer thickness (m)	No. layers	Growth rate	MFR cylinder
0.024	0.002	0.004	0.004	0.006	0.00075	6	1.0	3.1

Table 9
Current and wave generation at the inlet boundary.

Flow direction	Type of flow conditions		
	Uniform current flow	Profiled current flow	Wave and profiled current flow
U:	**u**$(x, y, z) = 0$ [ms^{-1}]	InletProf.Water. Velocity **u**(x,y,z)	InletProf.Water.Velocity **u** (x,y,z)
V:	**v**$(x, y, z) = 0$ [ms^{-1}]	InletProf.Water. Velocity **v**(x,y,z)	InletProf.Water.Velocity **v** (x,y,z) +VerticalParticleVelocity
W:	**w**$(x, y, z) = 1$ [ms^{-1}]	InletProf.Water. Velocity **w**(x,y,z)	InletProf.Water.Velocity **w** (x,y,z) +Horizontal Particle Velocity

numerical models.

Models incorporating regular waves (W1 or W2) had an additional input at the inlet of the domain, achieved by defining the surface wave elevation and the S2OT sub surface velocity components. The time-dependent wave velocity components were superimposed upon the preestablished steady state velocity profile.

The flow conditions in the flume can be presented as shown in Equation (5), where $w(t)$ is the instantaneous velocity in the streamwise direction, $\overline{W}$ is the time averaged velocity value, w' is the fluctuating component, and w_r is the wave orbital component.

$$w(t) = \overline{W} + w' + w_r \tag{5}$$

The addition of surface waves introduces an oscillatory component to the flow which increases the complexity of the flow regime and can have a significant impact on marine devices placed in these regions. Regular waves travelling in the same direction as the current flow will have a wave period (T_r), angular frequency (ω_r) and wave celerity (C_r) in a frame of reference that is moving at the same velocity as the average current ($\overline{W}$). In a stationary frame of reference, the waves will have a wave period (T_a), angular frequency (ω_a) and wave celerity (C_a). Waves induce oscillatory motions through a horizontal (w_a) and vertical (v_a) velocity component which are calculated in a stationary frame of reference using Equations (6) and (7) (Mani, 2012) where k is the wave number. Fig. 9 shows the key variables used to describe wave motion with the coordinate frame set with the z-axis in the direction of wave propagation, y-axis in the gravity direction and x-axis perpendicular to the YZ plane. The positional depth is referred to as 'y' with the Still Water Level (SWL) at $y = 0$ and the seabed at $y = -\ h$. The surface elevation (η) of the wave fluctuates around the SWL by a set amount known as the amplitude (a) of the wave, as detailed by Equation (8).

$$\begin{aligned} w_a &= \overline{W} + \frac{H}{2}\,\omega_r \frac{\cosh k\,(h+y)}{\sinh(kh)} \cos\,(kz - \omega_a t) \\ &+ \frac{3}{4}\left[\frac{\pi H}{L}\right]^2 C_r \frac{\cosh 2\,k(h+y)}{\sinh^4(kh)} \cos\,(2kz\ -\ 2\omega_a t) \end{aligned} \tag{6}$$

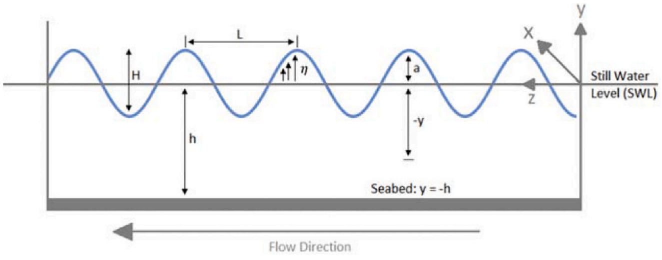

Fig. 9. Definition of wave motion.

$$\begin{aligned} v_a &= \frac{H}{2}\,\omega_r \frac{\sinh k(h+y)}{\sinh(kh)} \sin\,(kz - \omega_a t) \\ &+ \frac{3}{4}\left[\frac{\pi H}{L}\right]^2 C_r \frac{\sinh 2\,k(h+y)}{\sinh^4(kh)} \sin\,(2kz - 2\omega_a t) \end{aligned} \tag{7}$$

$$\eta = \frac{H}{2}\cos(kz - \omega_a t) + \frac{\pi H^2}{L}\frac{\cosh kh}{sinh^3 kh}(2 + \cosh 2\,kh)cos2(kz - \omega_a t) \tag{8}$$

The horizontal velocity component is superimposed upon the existing average current flow ($\overline{W}$). When this occurs, there is an interaction between the wave and current components which causes the angular frequency (ω_r) of the waves to change due to the Doppler shift (Galloway et al., 2010). This change can be observed in Equation (9).

$$\omega_r = \omega_a - k \cdot \overline{W} \tag{9}$$

The relative depth (h/L) of a wave is important in defining its characteristics, and can be classified as deep, intermediate or shallow (Henriques et al., 2016). The regular waves used in this study were intermediate depth water waves ($0.04 \leq h/L \leq 0.5$) with W1 having a relative depth of 0.221 and W2 of 0.357 as shown in Table 4. Intermediate water waves have circular velocity orbitals near the water surface, which become elliptical towards the seabed due to interaction between the water and the seabed as the water depth decreases.

4. Experimental and numerical results comparison

4.1. Turbine performance under current-only conditions

4.1.1. Flow characteristics

A comparison of the experimental and CFD current-only (U, P1 and P2) model results for the streamwise and vertical velocities are shown in Fig. 10. The bars on the experimental results represent ± 1 standard deviation either side of the mean. Experimentally, the biggest difference in the velocity over the water depth for the uniform current case was 0.01 m/s in the streamwise direction and 0.02 m/s in the vertical direction. The average standard deviation for the streamwise velocities were 0.009 m/s while the vertical velocities showed even less variation with a standard deviation of 0.003 m/s. The small differences in the velocity over the water depth and consistent standard deviation show that the flow conditions through the water depth were steady and uniform, validating the assumption that the flume possessed uniform current conditions.

Both P1 and P2 show a considerable reduction in the streamwise velocity towards the surface of the water, compared to the input flow velocity of 1.00 m/s, due to the presence of the wave maker. P1 has the greatest reduction in streamwise velocity near the water surface due to the wave maker being fully submerged to a depth of 50 cm in the top of the water column. P2 shows a smaller reduction in velocity as the wave maker was raised to a depth of 30 cm leading to less of a shearing effect through the water depth. Near the base of the flume, P1 has an increased streamwise velocity of 1.07 m/s to account for the reduction near the surface, while P2 maintains a velocity of 1.00 m/s. The experimental vertical velocity measurements for P1 and P2 show a constant velocity through the water depth with minor differences of 0.03 m/s for P1 and 0.01 m/s for P2 between the maximum and minimum velocities over the water depth. These values show a generally uniform vertical velocity exists for the profiled current cases, similar to the U case. The profiled current cases have a much greater standard deviation in the experimental results, particularly nearest the surface of the water, with P1 and P2 showing 0.060 m/s and 0.030 m/s, respectively, while a smaller standard deviation was observed towards the base of the flume, with P1 and P2 giving 0.012 m/s and 0.008 m/s, respectively. The standard deviation shows the unsteadiness in the water most likely due to vortex shedding in the flow from the stationary wave maker paddles. The standard deviation decreases towards the base of the flume where the

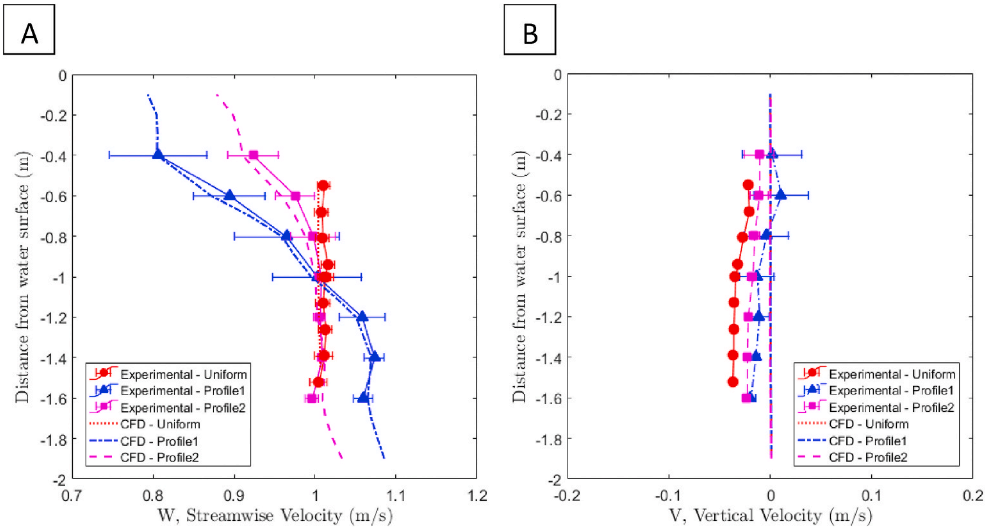

Fig. 10. The A) streamwise and; B) vertical, CFD and experimental velocity results, including the standard deviation, through the water depth for different current flow conditions. Bars show ± 1 standard deviation.

influence of the wave maker is less prominent.

The volumetrically averaged streamwise velocity over the turbine swept area ($\overline{W}_{vol}$) was calculated to provide a consistent estimate of the flow conditions upstream of the turbine. Initially, the $\overline{W}$ at each water depth was used in the calculation of the $\overline{W}_{vol}$; however, analysis of each velocity time series over the water depth showed that while the uniform flow cases were normally distributed, the profiled velocity results showed a negative skew. For a normally distributed data set, the most frequently occurring value (mode) and the central value of the data set (mean) occur at the same value. However, when a data set is skewed, there can be large differences between the values for the mean and mode. Fig. 11A shows a histogram of the LDA time series at a water depth of −0.55 m from the SWL for the U flow case where the mean and mode values are almost identical with a 0.1% difference. Fig. 11B and C show the histograms at a water depth of −0.4 m from the SWL for P1 and P2, respectively. The distributions show a much greater disparity between the mean and mode values, with a difference of 24% for P1 and 6% for P2, as shown in Table 10. For skewed data sets, the mean value is not representative of the predominant flow conditions at a specific water depth as it is the mode which is the most frequently occurring streamwise velocity. To account for these differences in the distributions, the $\overline{W}_{vol}$ was recalculated using the mode instead of the mean values, as shown in Table 11. This alternative method of calculating the $\overline{W}_{vol}$ has a negligible effect on normally distributed data; however, for skewed data sets P2 gives a 0.3% difference when using the mode to calculate the $\overline{W}_{vol}$, while P1 shows a 4% difference. The mode is therefore recommended for use in all following flow analyses as this value is more representative of skewed data sets but remains the same as the mean value in normally distributed data sets.

Table 10
The experimental mean, mode and difference of each histogram displayed in Fig. 11.

Type of flow	Average streamwise velocity, $\overline{W}$			
	Mean (m/s)	Mode (m/s)	Difference	
			(m/s)	(%)
U	1.011	1.010	0.001	0.1
P1	0.806	1.000	0.194	24.0
P2	0.924	0.980	0.056	6.0

Table 11
Experimental volumetrically averaged streamwise velocities calculated using the mean and mode.

	Volumetrically averaged streamwise velocity over turbine swept area ($\overline{W}_{vol}$), calculated using…		Difference	
	Mean (m/s)	Mode (m/s)	(m/s)	(%)
U	1.011	1.012	0.001	0.1
P1	1.004	1.042	0.038	4
P2	1.001	1.004	0.003	0.3

The CFD model results show good agreement to the flow results obtained experimentally, as shown in Table 12. The streamwise and vertical velocity results (Fig. 10) show a difference of <2% of the $\overline{W}_{vol}$ for all cases, apart from the U case vertical velocity which shows

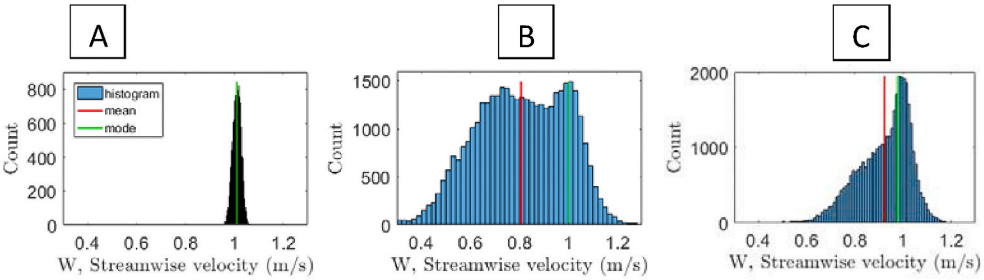

Fig. 11. Histograms showing the mean and mode of experimental LDA data sets at a water depth of −0.55 m, −0.4 m and −0.4 m for A) U, B) P1 and C) P2 flow conditions, respectively.

Table 12
$\overline{W}_{vol}$ in uniform and profiled flow conditions for the experimental and CFD model results.

Case	Volumetrically averaged streamwise velocity over swept area of the turbine, $\overline{W}_{vol}$ (m/s)	
	Experimental	CFD
U	1.01	1.00
P1	1.04	0.99
P2	1.00	0.99

differences up to 4%. These differences between the experimental and CFD streamwise velocity are small, confirming that the velocity profile imposed at the inlet of the CFD model has been maintained downstream and is therefore applying the appropriate flow conditions at the turbine location. The differences in the vertical velocity results are also small, however, the CFD model fails to develop fluctuations in the vertical velocity profile as seen in the experimental results, leading to a vertical velocity of 0.00 m/s for all flow cases. The streamwise velocity dominates the flow field and therefore variations in the vertical velocity input at the inlet have disappeared by the time the flow is measured 1 m upstream of the turbine location. The experimental vertical velocity fluctuations could be due to intrinsic flume turbulence (Gaurier et al., 2020b); features which were not replicated in the CFD model as use of higher order modelling techniques would be necessary, ie. Detached Eddy Simulation (DES) or Large Eddy Simulation (LES) (Ebdon, 2019).

4.1.2. Turbine characteristics

Due to the squared and cubic relationships of the $\overline{W}_{vol}$ used in the calculation of the performance characteristics, a small under or over estimation in this value will result in an amplified error in the calculation of C_q, C_t, and C_p. For example, the experimental performance characteristics for P1, P2 and U showed 8–12%, 1% and 0.2% difference, respectively, when using the $\overline{W}_{vol}$ calculated with the mean or mode. These results show that the distribution of the velocity data sets can have a significant effect on the calculation of the performance characteristics when using the mean value and emphasises the importance of accurately estimating the inflow velocity to the TST.

Fig. 12 shows the performance characteristics, C_q, C_t, and C_p, for the experimental results over a range of TSRs, the uniform CFD results also over the full range of TSRs, and the profiled CFD results at only a TSR of 4. The average values for each of the performance characteristics show good agreement across all three of the flow cases. The maximum difference between the average C_q, C_t, and C_p for each of the flow cases in the peak power region (3≤TSR ≤5) was 0.01, 0.06 and 0.04, respectively. These differences are all <10% and are considered small,

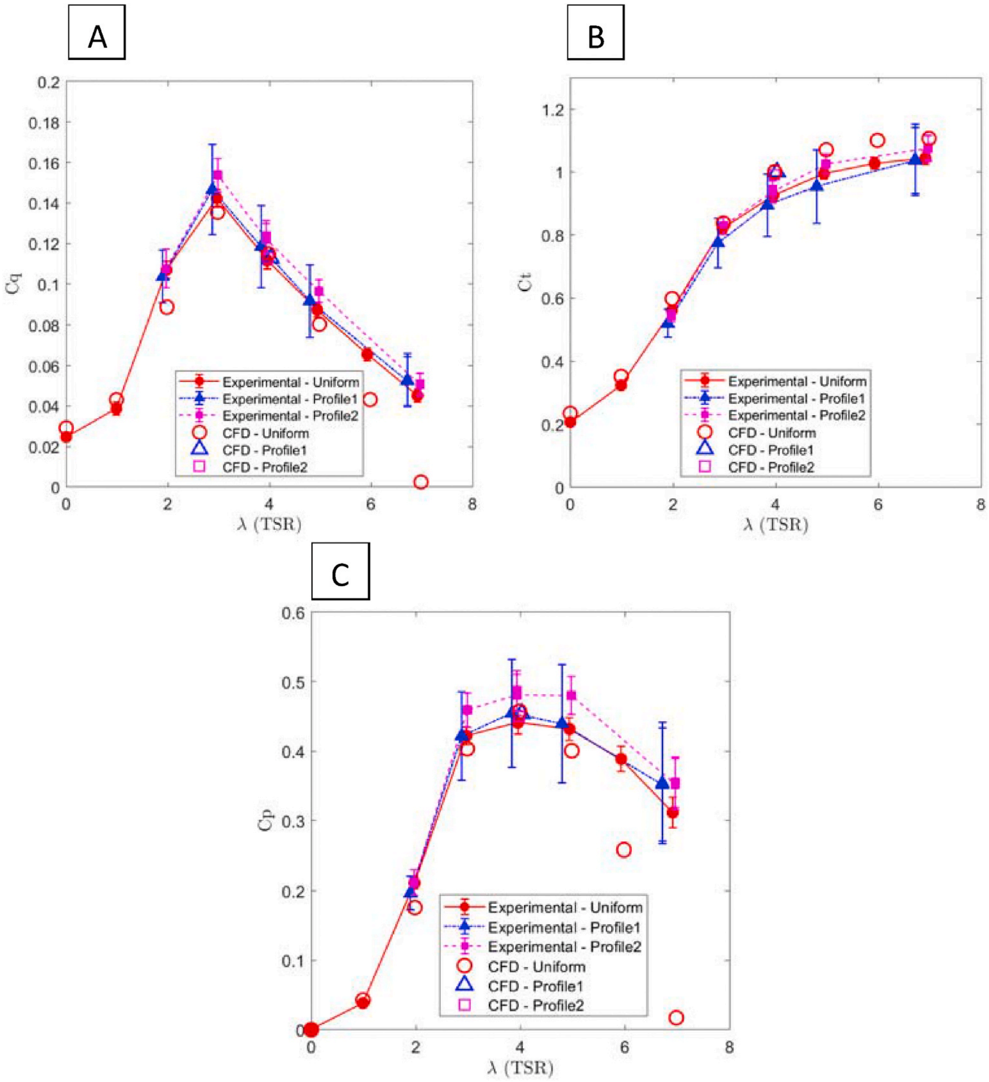

Fig. 12. The A) C_q, B) C_t and C) C_p for the experimental and CFD results in uniform and profiled flow conditions, calculated using the mode instead of the mean for the $\overline{W}_{vol}$. Bars show ± 1 standard deviation.

especially as the mean values for each data set are within the limits of the standard deviation bars of the other data sets. For all flow cases, the performance characteristics estimated by the CFD models show good agreement with the experimental results, lying within 1 standard deviation of the average. Table 13 shows the average experimental and CFD results for each performance characteristic at a TSR of 4, as well as the difference between them.

Experimentally, there is also significant differences in the standard deviation of the data sets between the uniform and profiled current cases. P1 has the biggest average standard deviation around the mean for all performance characteristics giving an average standard deviation of 0.02, 0.09 and 0.07 for C_q, C_t and C_p, while P2 gives 0.01, 0.03 and 0.03 and U has 0.01, 0.02 and 0.02, respectively. The presence of the wave maker when fully submerged causes a high level of disturbance to the current flow. Raising the wave maker by 20 cm reduces the unsteadiness in the flow, while removing it completely, as seen in the U flow case, results in a significant reduction in the flow disturbances. These differences in the wave maker positioning can clearly be seen in the difference of the standard deviation around the mean for each of the performance characteristics.

To further validate the current-only CFD models, the BM*x* on the turbine blades were compared with the experimental data. A single turbine blade was analysed as the same trends were present on each of the three individual blades, although each offset by 120°. An initial comparison analysing the average BM*x* showed good agreement between the data sets, as shown in Table 14.

The experimental BM*x* time series possessed unsteady flow features such as turbulence and unwanted noise which interfered with the measurement signal, unlike the CFD simulations which were conducted in controlled conditions. The unsteadiness in the experimental results made it difficult to directly identify specific patterns and features and therefore Time Synchronous Averaging (TSA) was used to average the BM*x* fluctuations over multiple rotational cycles of a turbine blade. TSA reduces the effect of noise on the signal and highlights the underlying cyclic BM*x* fluctuations over a single turbine rotation, as shown in Fig. 13. This method has been proven to be effective in turbine performance characterisation without adversely affecting the frequency domain representations of the loadings developed (Allmark et al., 2017).

The experimental BM*x* results for the U flow case show a relatively steady velocity leading to a low noise content as shown in Fig. 13Ai). The average amplitude of fluctuation in the BM*x* is 0.45 Nm for the U flow case due to stanchion interaction with each turbine blade. Increasing levels of unsteadiness in the flow can be observed in Fig. 13Bi) and Fig. 13Ci) which reflect changes in the flow characteristics, for P1 and P2, induced by the presence of the wave maker. This causes the average amplitude of fluctuation in the BM*x* to increase to 0.76 Nm for P2 and 2.25 Nm for P1 as the fluctuation is directly related to the shearing gradient in the velocity profile. The same trend exists for the CFD BM*x* results; however, due to turbulence dissipation there is no noise present in the numerical simulation which leads to repeatable time series producing a much cleaner signal. The experimental and CFD results show good agreement between the average BM*x* for all cases (Table 14) as well as the average amplitude of fluctuation in the BM*x* for P1 and P2, as shown in Table 15.

Table 14
The average CFD and experimental BM*x* results in uniform and profiled flow conditions.

Case	Average out of plane bending moment, BM*x* (Nm)		
	Experimental	CFD	Difference
U	23.99	24.24	0.25
P1	25.20	23.73	1.47
P2	24.68	23.53	1.15

4.2. Turbine performance under wave-current conditions

4.2.1. Flow characteristics

The addition of a wave characteristic to each of the existing profiled current flows has a minor effect on the average velocity over the water depth with a maximum difference between cases of <5%. Fig. 14 shows a comparison of the experimental and CFD model results for the average streamwise and vertical velocities given by each of the wave-current cases. The greatest difference between the experimental and the CFD results for the streamwise and vertical velocities at each water depth was <2.5% of the $\overline{W}_{vol}$, even though the vertical velocity results given by the CFD models do not develop the same profile as the experimental results. Nevertheless, the experimental and CFD $\overline{W}_{vol}$ over the turbine swept area for each case were within 4% of one another, as shown in Table 16, and therefore deemed acceptable.

Fig. 15 and Fig. 16 show how the addition of a wave characteristic induces an oscillatory wave orbital velocity component around the average current flow. These figures compare the experimental and CFD model results when operating under the conditions given by P1W1 and P2W2, respectively. For both wave cases, the amplitude of oscillation around the average current flow is greater towards the water surface, decaying as the wave motion penetrates through the water depth, for both the streamwise and vertical wave induced velocities, as shown experimentally in Table 17. The wave induced fluctuations for the streamwise and vertical velocities in the P2W2 case are greater than the P1W1 case in the top half of the water column. However, the wave induced oscillatory effects decay quicker in the P2W2 case; this is because the oscillatory motions of a wave can penetrate the water column by up to half the wavelength (Sorensen, 2006) and P1W1 has a greater wavelength of $L = 9.07$ m in comparison to P2W2 which has $L = 5.61$ m. Both wave cases are intermediate water waves so still have a significant vertical and horizontal velocity component at the base of the flume. The turbine will therefore be subjected to considerable loads, and fluctuations in these loads, in both the horizontal and vertical directions throughout the 2 m water depth.

The CFD streamwise velocity results show good agreement with the experimental data, however, the vertical velocities have a larger discrepancy between the two data sets, particularly towards the bottom of the water column. Whilst the wave induced fluctuations in the vertical velocity are comparable to the experimental values, the CFD model does not reproduce the profiled gradient of the average experimental vertical velocities.

The magnitudes of the wave induced velocity fluctuations are shown in Fig. 17A and Fig. 18A. The experimental and the CFD data sets show very good agreement, with the greatest difference being <1% of the $\overline{W}_{vol}$ for both wave-current cases. The wave induced oscillations fluctuate

Table 13
The experimental and CFD results for C_q, C_t and C_p, in uniform and profiled flow conditions at TSR 4.

Profile	C_q			C_t			C_p		
	Exp.	CFD	Dif.	Exp.	CFD	Dif.	Exp.	CFD	Dif.
U	0.112	0.115	0.003	0.928	1.001	0.073	0.443	0.457	0.014
P1	0.118	0.113	0.006	0.895	1.000	0.105	0.455	0.454	0.001
P2	0.122	0.113	0.009	0.938	0.992	0.054	0.481	0.449	0.032

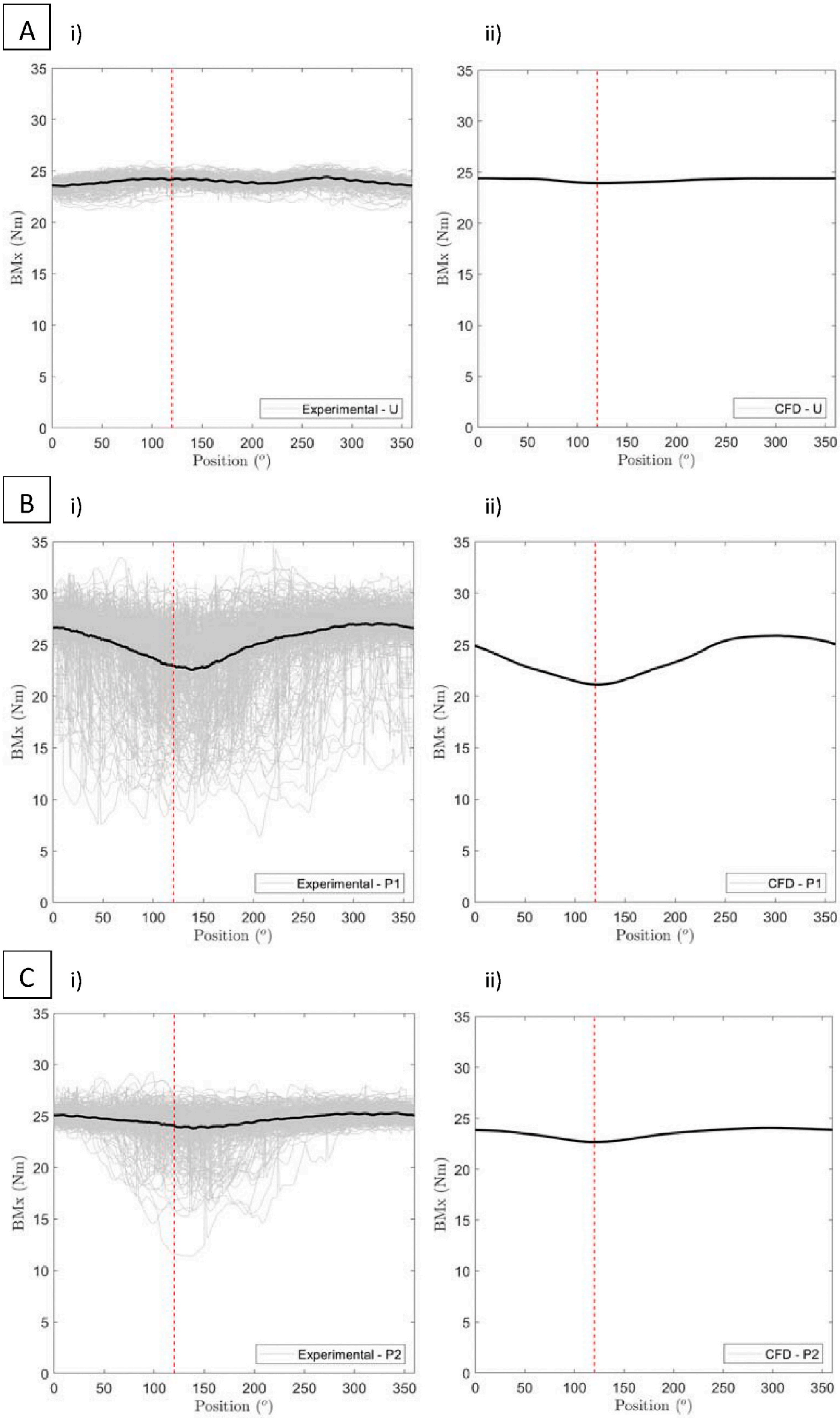

Fig. 13. The average i) experimental and ii) CFD BM*x* fluctuation on a single blade calculated using TSA for A) U, B) P1, and C) P2 current conditions. [Red dotted line shows position of blade TDC at 120.°]

Table 15
The amplitude of fluctuation in the experimental and CFD BMx calculated using the TSA method.

Case	Amplitude of fluctuation in the out of plane bending moment using TSA method, BMx (Nm)		
	Experimental	CFD	Difference
U	0.45	0.24	0.21
P1	2.25	2.37	0.12
P2	0.76	0.70	0.06

around the current velocity with the same magnitude, regardless of whether a uniform or profiled velocity gradient exists (Lloyd et al., 2019b). For the conditions given by P1W1, a single turbine blade experiences a maximum difference of 0.32 m/s in the streamwise velocity as it passes through the different flow regions over the rotational cycle, with a velocity of 0.82 m/s at TDC and 1.14 m/s at Bottom Dead Centre (BDC). In comparison, P2W2 has a difference of 0.24 m/s over the rotational cycle, with a velocity of 0.85 m/s at TDC and 1.09 m/s at BDC. The current profile that the wave characteristic is superimposed upon will affect the amount of shear across the water depth and consequently the loadings imposed on the turbine. The combination of wave and current interaction together will have a significantly greater effect across the turbine, as opposed to current or wave-only conditions.

Figs. 17B and 18B show the wave orbital components in the vertical direction for P1W1 and P2W2 with their average values subtracted. This data shows that for the vertical wave orbital components, good agreement is displayed by the experimental and CFD results for both wave-current cases. It is the differences in the average velocities which offsets the wave orbital components and therefore appears to agree less well. All vertical velocity CFD results are within 1 standard deviation of the equivalent experimental values apart from at a distance from the SWL of −0.8 and −1.2 m in the P2W2 case. However, at this water depth the greatest difference between the experimental and CFD results is <2%.

The surface elevation of the wave was measured at the turbine rotor plane ($z = 3.88$ m) which gave a clear indication of the wave surface profile and allowed a direct comparison between the wave elevation and the induced turbine loadings. Fig. 19 and Fig. 20 show the wave surface elevation over a 5 s time period for the experimental and CFD model results of P1W1 and P2W2, respectively. Experimentally, Figs. 19 and 20 show a 5 s snapshot of the total data set; however, both the wave frequency and wave height were measured over 7 to 10 different tests and an average was obtained across the multiple runs to get a more representative average of the sample conditions. Table 18 shows the target and measured wave characteristics for the experimental results as well as the CFD model comparison. The measured experimental results show good agreement to the target values input to the wave maker, with <1% difference in the wave frequency. The measured wave height for both cases are within 9% of the target values showing the variability present in this measurement. A dominating current flow along with strong velocity variations induced by the surface waves caused deflection of the wave probes during the experimental testing. These flow characteristics contribute to the unsteadiness of the readings but are hard to quantify.

Table 16
Volumetrically averaged streamwise velocity for the experimental and CFD model results.

Profile	Volumetrically averaged streamwise velocity over swept area of the turbine, $\overline{W}_{vol}$ (m/s)		Difference	
	Experimental	CFD	(m/s)	(%)
P1W1	1.046	1.009	0.037	3.7
P2W2	1.052	1.021	0.031	3.0

The CFD results show stability after 40 s of run time and therefore show a repeating pattern after this point has been reached, with a wave height of 0.081 m and 0.12 m for the conditions represented by P1W1 and P2W2, respectively. These values show good agreement with the experimental results, with only 1.3% difference for P1W1 and no difference in the average value for P2W2. The CFD average wave frequency and wave height are both <3% of the experimental values.

Overall, the CFD simulations accurately reproduce the wave and current conditions generated at the IFREMER flume experimentally. The differences between the experimental and CFD average velocity and wave orbital velocities are <3% of the $\overline{W}_{vol}$. The wave surface elevation produced by the CFD model is within 2% of the experimental results, and the wave frequencies show <3% difference. Fig. 21 shows the instantaneous flow conditions generated by the P2W2 CFD model, as well as indicating the position of the wave crests.

4.2.2. Turbine characteristics

Fig. 22 shows the experimental C_q, C_t, and C_p for the five test cases, calculated using the $\overline{W}_{vol}$ to account for the differing velocity profiles over the swept area of the turbine, as detailed in Table 16. Strong agreement was found between the P1W1 and P2W2 flow cases for each of the performance characteristics, with a maximum difference of 2%,

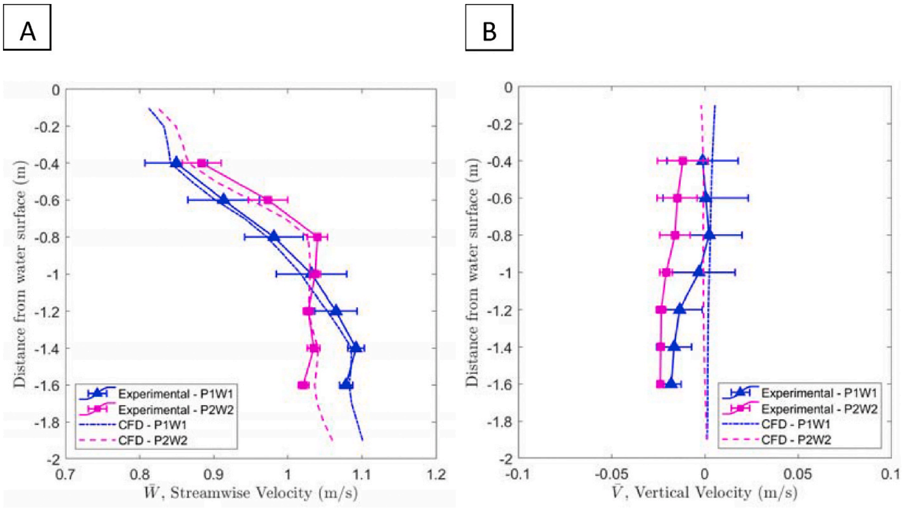

Fig. 14. The average A) streamwise and; B) vertical, CFD and experimental velocity results through the water depth for P1W1 and P2W2. Bars show ± 1 standard deviation.

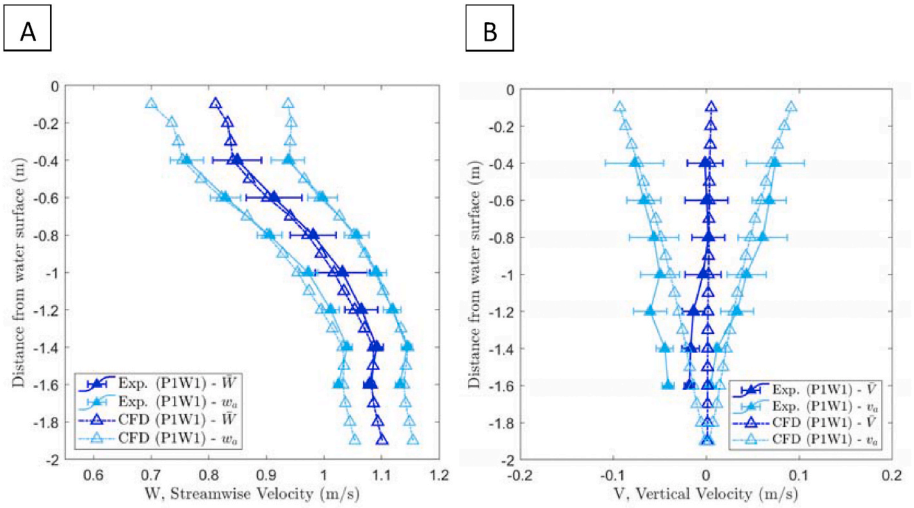

Fig. 15. For P1W1, the average and wave orbital A) streamwise and; B) vertical, CFD and experimental velocity results. Bars show ± 1 standard deviation. [$\overline{W}$or $\overline{V}$ = average velocity, w_a or v_a = maximum and minimum wave orbital velocity component].

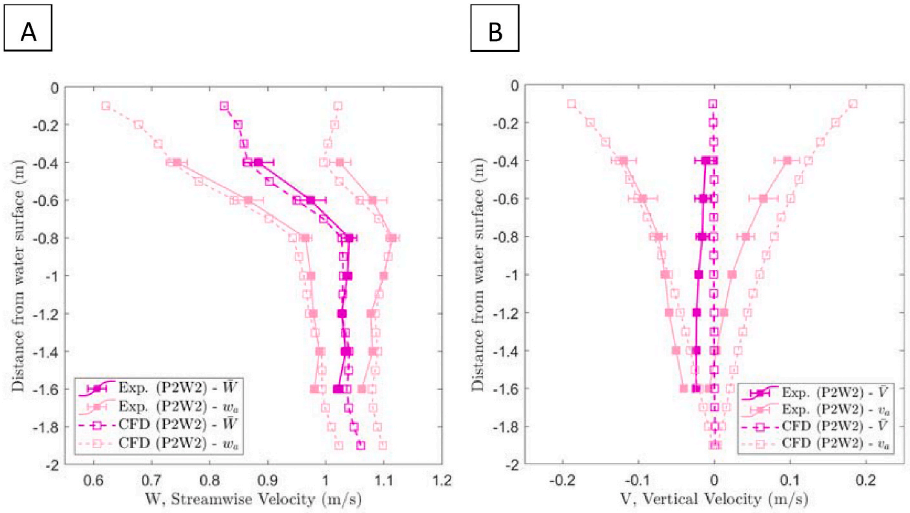

Fig. 16. For P2W2, the average and wave orbital A) streamwise and; B) vertical, CFD and experimental velocity results. Bars show ± 1 standard deviation. [$\overline{W}$or $\overline{V}$ = average velocity, w_a or v_a = maximum and minimum wave orbital velocity component].

Table 17
Experimental wave induced velocity fluctuations, measured at points through the water column.

Distance from water surface (m)	Amplitude of fluctuation around mean velocity value (m/s)			
	P1W1		P2W2	
	Streamwise	Vertical	Streamwise	Vertical
−0.4	0.09	0.08	0.14	0.1
−1.0	0.06	0.05	0.06	0.04
−1.6	0.05	0.02	0.04	0.02

2% and 4% for C_q, C_t, and C_p, respectively, over the peak power region (3<TSR<5). Good agreement was also found between the average performance characteristics for the wave-current and current-only cases with the maximum difference for C_q, C_t, and C_p < 10%. Table 19 shows the performance characteristics for each of the flow cases at peak power, TSR 4, showing the repeatability of the performance characteristics over a range of flow characteristics.

Table 20 shows a comparison of the CFD and experimental average performance characteristics for the wave-current cases at a TSR of 4. The C_q, C_t and C_p estimated by the CFD model at a TSR of 4 show good agreement with the experimental results, all lying within 1 standard deviation of the average value and having a maximum difference of <10%.

The BM*x* for a single turbine blade was compared experimentally and numerically to further analyse the transient behaviour of the turbine under wave-current conditions. As described in Section 4.1.2, the dominating fluctuation in the BM*x* for the current-only cases was due to stanchion interaction and the impact of the velocity profiles with each turbine blade every rotation. The introduction of waves incorporates an additional fluctuating component that affects the turbine loadings, as shown by Fig. 23.

Under P1W1 conditions, each turbine blade completes a full rotation every 0.7 s and interacts with the stanchion once during this time (Fig. 23A). The wave period of W1 is 2.0 s and therefore every 14 s the turbine will rotate 20 times while 7 waves propagate past the turbine.

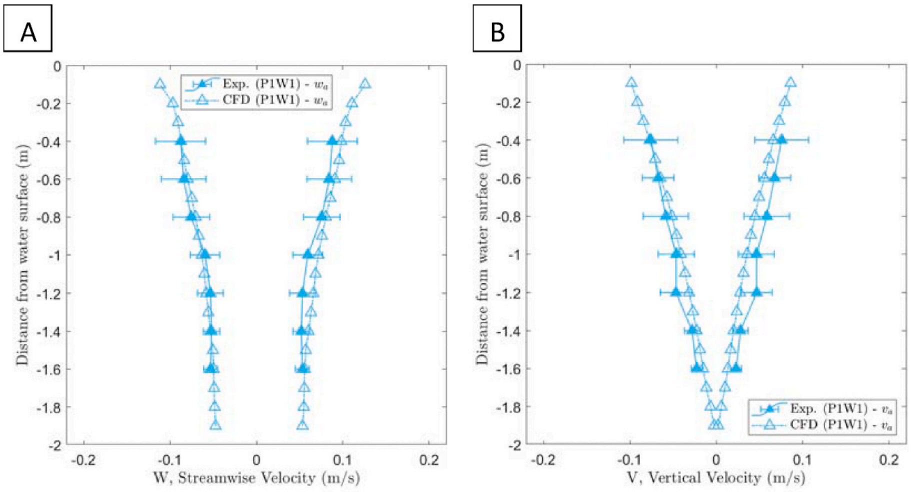

Fig. 17. For P1W1, the wave orbital components for the A) streamwise and; B) vertical, CFD and experimental velocity results. Bars show ± 1 standard deviation. [w_a or v_a = wave orbital velocity component].

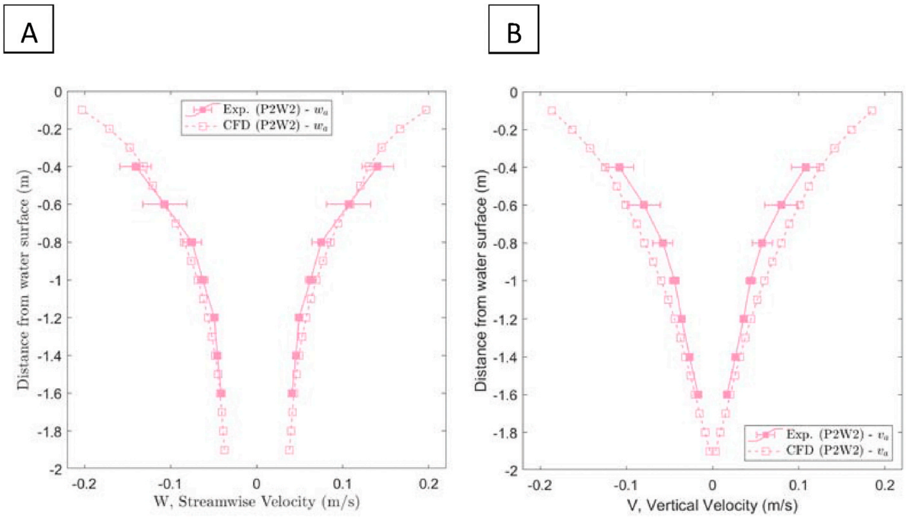

Fig. 18. For P2W2, the wave orbital components for the A) streamwise and; B) vertical, CFD and experimental velocity results. Bars show ± 1 standard deviation. [w_a or v_a = wave orbital velocity component].

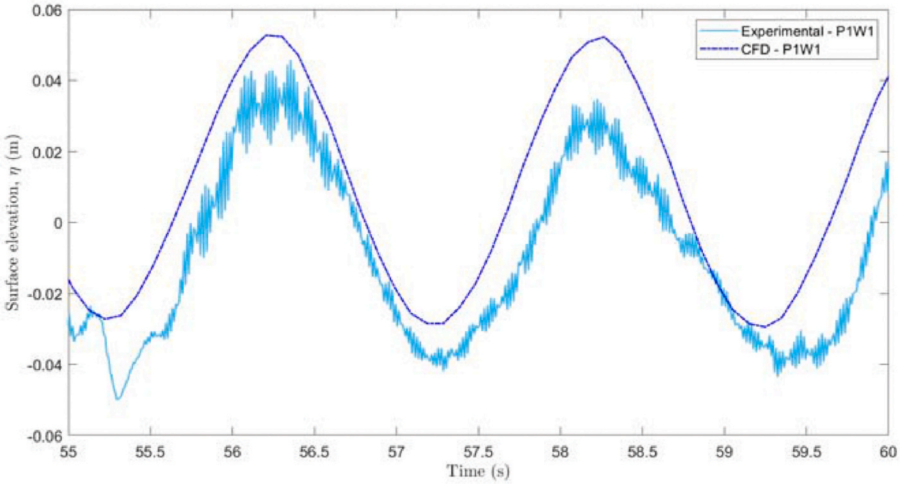

Fig. 19. The experimental and CFD surface elevation for the conditions given by P1W1.

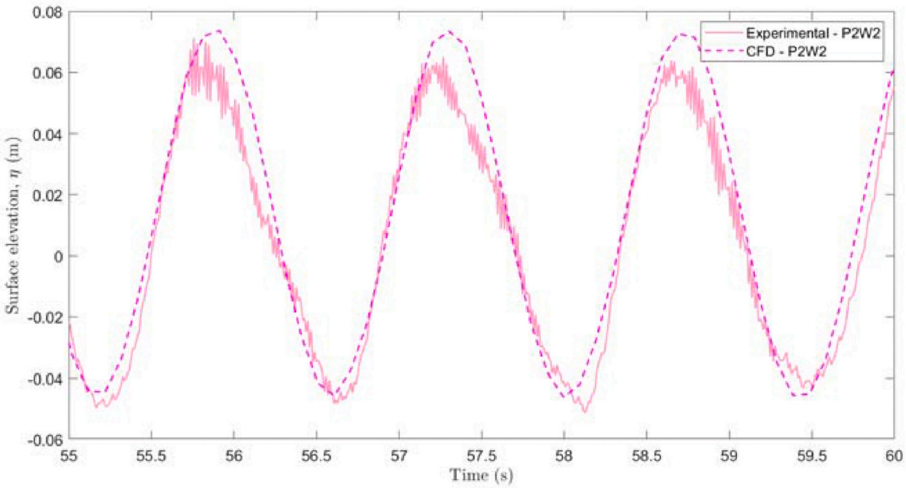

Fig. 20. The experimental and CFD surface elevation for the conditions given by P2W2.

The rotational frequency and the wave frequency result in a combined fundamental period of 14 s, where the transient BM*x* alters over this 14 s window, however, each 14 s window will repeat the same pattern. This window has been marked on Fig. 23 to show the repeating envelope, while the rotational frequency is marked with a red arrow and each wave period is marked with a green arrow.

For the P2W2 case, the time taken for a blade to do a single rotation is again 0.7 s, while the wave period of W2 is 1.43 s (Fig. 23B). For this case, the wave frequency is almost twice the rotational frequency and therefore both components are essentially in phase with one another. This results in the BM*x* fluctuation being dominated by the wave interaction and only a small drop in the BM*x* can be seen due to the turbine blade interacting with the stanchion and differing flow velocities each full rotation.

The TSA method was applied to reduce the noise in the wave-current time series and to accentuate the underlying fluctuations in the BM*x* results. Table 21 shows the average experimental and CFD BM*x* values which show good agreement between the cases. Fig. 24 shows the average experimental and CFD BM*x* on a turbine blade calculated using TSA, with the corresponding wave surface elevation positioned underneath for P1W1 and P2W2. The maximum and minimum fluctuation in the BM*x* coincides with the peak and trough of the wave surface elevation, respectively. This is shown both experimentally and numerically showing strong similarities between the shape and magnitude of fluctuation in the BM*x*.

These transient results, however, consist of multiple combined frequencies such as interaction with the stanchion and velocity profile at the rotational frequency, and interaction with regular waves at the wave frequency. A Fast Fourier Transform (FFT) was therefore conducted to decompose the time series into its dominant frequencies and quantify the magnitude of fluctuation in the BM*x* created by stanchion and wave interactions with the turbine.

Fig. 25 shows the FFT analysis for the experimental and CFD BM*x* results for each wave-current characteristic at a TSR of 4. The red arrows mark the rotational frequency of the turbine, showing the combined interaction of the stanchion and velocity profile with a turbine blade, while the green arrows mark the wave frequency. For both wave-current cases, there are two peaks situated at the wave and rotational frequencies. The peak at the rotational frequency (1.4 Hz), for both P1W1 and P2W2, shows good agreement with the amplitude of fluctuation in the BM*x* seen in the current-only cases of P1 and P2, respectively, as shown in Table 22. This shows that the interaction of each turbine blade with the stanchion and velocity profile is the same regardless of the wave characteristics superimposed on the profiled current velocity. The velocity profile in P2W2 is less shearing across the water depth than in P1W1, resulting in a smaller fluctuation in the BM*x* at the rotational frequency. This observation agrees with analysis of the profiled current-only conditions, as shown in Tables 15 and 22.

The wave frequency of P2W2 shows a much greater amplitude of fluctuation in the BM*x* in comparison to the rotational frequency, while in P1W1 both the wave and rotational frequency components have a similar amplitude of fluctuation. This emphasises the considerable effect that a velocity profile across the water column can have on the loading fluctuations of the turbine. Table 22 shows that the uniform current-only case has the smallest amplitude of fluctuation in the BM*x* of $<$0.5 Nm. There are no waves or profiled velocity gradients, therefore, the fluctuation in the BM*x* is solely due to interaction with the stanchion each rotation. P2 introduces a small amount of shear to the current velocity through the water depth which increases the amplitude of fluctuation to $\approx$0.7 Nm. A further increase in the amount of shear in the current velocity (P1) has a significant effect on the fluctuation in the BM*x*, reaching a magnitude of $\approx$2.4 Nm. Both the wave-current cases, P1W1 and P2W2, induce an amplitude of fluctuation in the BM*x* at the wave frequency of $\approx$2.2–2.7 Nm, similar to the amplitude of fluctuation caused by P1. Therefore, a highly shearing velocity profile, such as P1, can have just as big an effect as the wave induced loadings of W1 and W2 experienced in this study.

An equally important factor to consider is the phase of the wave in comparison to the position of a turbine blade in its rotational cycle. If these two components are in phase, this can substantially increase the magnitude of the loading fluctuations that a single turbine blade experiences, as found by (Ordonez-Sanchez et al., 2016). However, when these components are out of phase, the impact of the loading fluctuations would be more frequent, but with a smaller magnitude. It is important to minimise large loading fluctuations and therefore control strategies can be developed and used to monitor incoming waves and adjust the turbine rotational speed to optimise the blades position in comparison to the waves (Ordonez-Sanchez et al., 2016).

The CFD models, shown by Fig. 25ii), reproduce the results observed experimentally to within ± 1 standard deviation, showing good agreement between the data sets. Both sets of results found that W2 has a greater effect on the amplitude of fluctuation in the BM*x* of a turbine blade in comparison to W1.

Validation of CFD models, using uniform and profiled current-only conditions as well as combined wave-current characteristics, has been successfully achieved for a 1/20th scale TST in the peak power operational region. The CFD models reflect the experimental conditions to within 1 standard deviation for multiple flow and turbine parameters,

Table 18
A summary of the target, experimental and CFD model wave frequencies and wave heights.

	Mean value (±1 standard deviation)					
	P1W1			P2W2		
	Target	Experimental	CFD	Target	Experimental	CFD
Wave frequency, f (Hz)	0.5	0.5 ± 0.003	0.49	0.7	0.7 ± 0.001	0.72
Wave height, H (m)	0.09	0.082 ± 0.009	0.081	0.11	0.12 ± 0.008	0.12

such as turbine performance characteristics, streamwise and vertical velocity data, wave surface elevation, and BMx blade loadings. Further analysis can now be carried out to investigate transient loading features as a result of the different flow conditions.

4.3. CFD comparison of transient turbine loadings: current-only and wave-current

Blade, hub and total turbine thrust and torque loadings were investigated using CFD simulations as individual component loadings were not measured during the experimental testing. It is therefore assumed that the data presented by the CFD models would be representative of the experimental thrust and torque data as a result of prior validation using alternative parameters. The average thrust and torque loadings show good similarity between each of the five types of flow condition tested (U, P1, P2, P1W1, P2W2), with small variations between cases due to differences in the calculated $\overline{W}_{vol}$. Table 23 shows how these average thrust and torque loadings are not significantly affected by the different wave and current characteristics.

Fig. 26 shows the transient thrust and torque loadings for a single blade, the hub and the turbine total for each of the five test cases (U, P1, P2, P1W1, P2W2). The surface elevation of the two wave cases (W1 and W2) are also shown in Fig. 26iv) to demonstrate comparisons between the surface elevation and loadings experienced for the wave-current cases. Fig. 26Ai) shows that for the current-only cases, the transient cycle of the thrust on each turbine blade is repeated, with the peak and trough of the results aligned with the rotational frequency of the turbine (0.7 s). The amplitude of fluctuation around the average thrust is 1.03 N, 10.02 N and 2.65 N for U, P1 and P2, respectively, which shows that the fluctuation in the thrust on a single turbine blade for P1 is 3 times that of P2, and 10 times the U flow case. For the wave-current cases, the loading fluctuations experienced by a single turbine blade is a complex combination of interactions between the rotational speed of a blade passing the stanchion, the amount of shear in the velocity profile, and the propagating surface waves. The amplitude of fluctuation around the average thrust is 10.91 N and 12.48 N for P1W1 and P2W2, respectively, which is similar to the fluctuation in the thrust for P1. Such a finding confirms that shear induced flow structures, as well as wave induced conditions, will be significant drivers of loading perturbations and must be quantified to correctly design TST structures.

The transient torque loadings for a single turbine blade in current-only conditions show a similar trend to the thrust loadings, as shown in Fig. 26Bi). The amplitude of fluctuation around the average torque is 0.79 Nm, 1.39 Nm, 0.86 Nm, 1.14 Nm and 1.49 Nm for U, P1, P2, P1W1 and P2W2, respectively. The fluctuation in the torque on a single blade is greatest for the highest shearing velocity (P1) and the wave cases. Again, the different flow conditions have a negligible effect on the average torque on a single blade but does affect the fluctuation around the average value. There are small discrepancies between the phase of the cyclic loadings for each of the flow cases as the angular velocity of the turbine was set to reflect the results obtained experimentally, resulting in minor changes between the rotational period of the turbine.

Fig. 26Aii) and Fig. 26Bii) show the respective thrust and torque on the hub for each of the flow cases tested. The presence of a velocity profile has a negligible effect on the fluctuation of the thrust and torque on the hub, as seen for cases U, P1 and P2. The hub is static in the water column and at a central depth where the streamwise velocity for all cases is 1.00 m/s. It would be expected that the loadings imparted on the hub for all flow conditions are similar; however, the introduction of surface waves increases the fluctuation in the thrust to ≈1.2 N while the amplitude of fluctuation in the thrust without waves was <0.05 N. The surface waves did not affect the fluctuation in the torque, however, remaining close to 0 Nm.

Fig. 26Aiii) shows the significant difference observed for flow cases with and without waves in the total turbine (all blades and hub) transient thrust results. When summing to calculate the total turbine loadings, the fluctuation observed in the thrust on a single turbine blade is cancelled out due to each blade being 120° out of phase with one another. Therefore, when the individual loadings are summed, the amplitude of fluctuation is significantly reduced. It is still critical to account for the stanchion interaction with each turbine blade, in terms of blade design, fatigue life and manufacture; however, this fluctuation

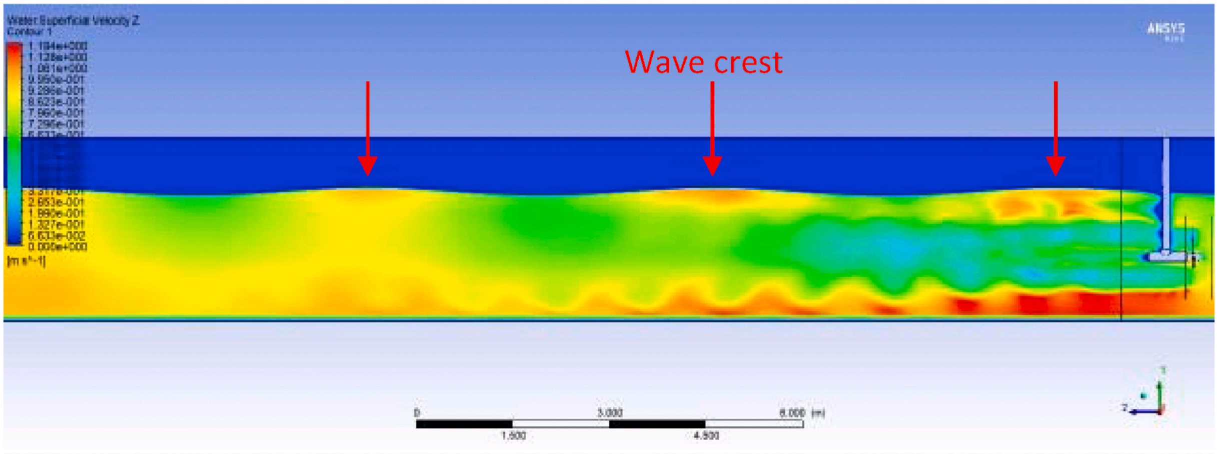

Fig. 21. The instantaneous streamwise velocity when the turbine is operating at a TSR of 4 for the inlet wave and current conditions representative of P2W2.

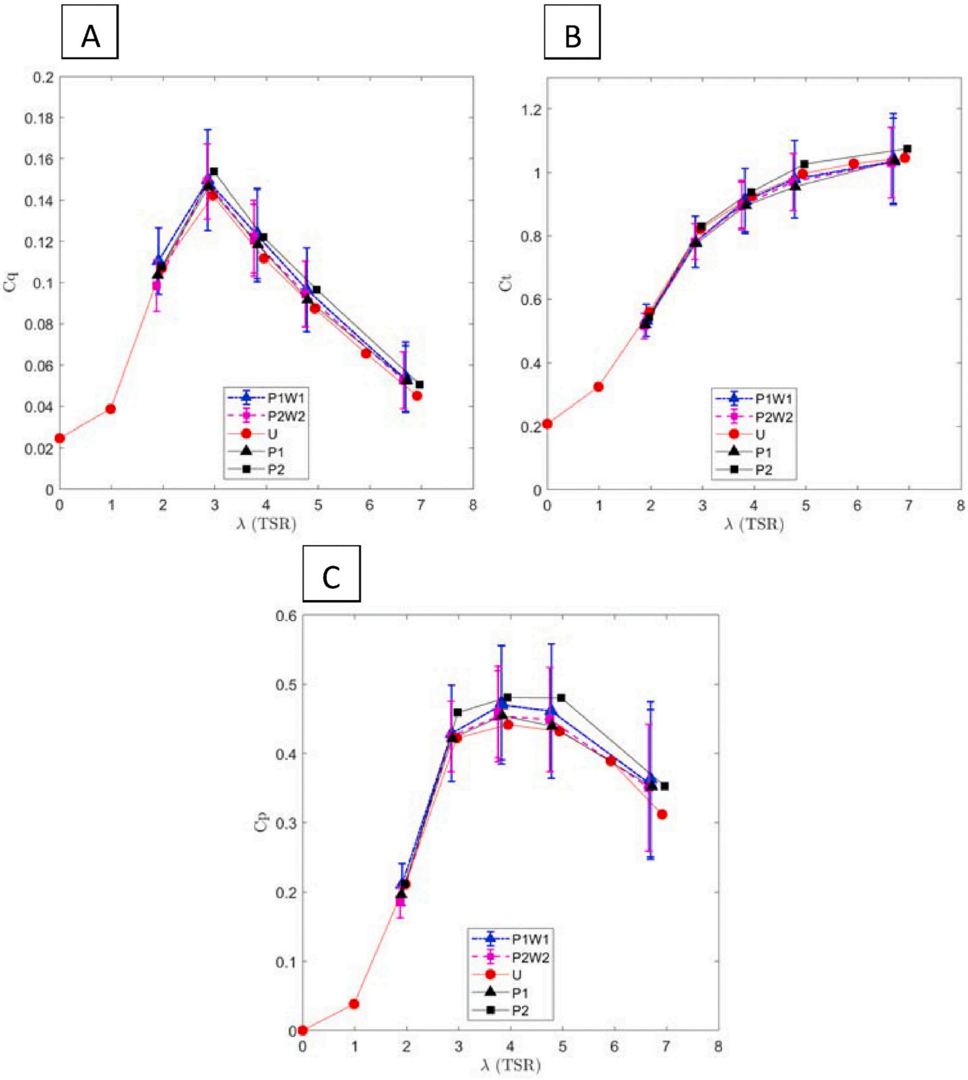

Fig. 22. The A) C_q, B) C_t and C) C_p for the experimental results in wave-current conditions (P1W1, P2W2) compared against current-only conditions (U, P1, P2). Bars show ± 1 standard deviation.

Table 19
Values for the experimental performance characteristics at a TSR of 4.

Performance characteristic	U	P1	P2	P1W1	P2W2
C_q	0.11	0.12	0.12	0.12	0.12
C_t	0.93	0.90	0.94	0.91	0.89
C_p	0.44	0.45	0.48	0.47	0.45

is not visible in the total turbine loading results. These results emphasise the importance of analysing the turbine component loadings individually as well as in a combined total. The amplitude of fluctuation around the average total thrust for the current-only cases is 0.28 N, 0.19 N and 0.74 N for U, P1 and P2, respectively, as shown in Table 24. When surface waves are introduced, the amplitude of fluctuation around the average total thrust increases to 33.6 N and 37.8 N for P1W1 and P2W2, respectively, which is around 35 times greater than the fluctuation in the current-only cases. The maximum and minimum peaks in the transient total thrust results directly coincide with when a crest or trough of the wave propagates past the turbine, as shown in Fig. 26Aiv).

A similar trend is observed in the transient total torque results, as shown in Fig. 26Biii). The amplitude of fluctuation around the average total torque is 0.02 Nm, 0.02 Nm and 0.07 Nm for U, P1 and P2, respectively, as shown in Table 24. The amplitude of fluctuation for P1W1 and P2W2 are 3.39 Nm and 3.92 Nm, respectively, which is again about 35 times greater than the fluctuation in the current-only results. The fluctuation in the loadings is significantly greater for the cases incorporating waves than without, and peaks in the loadings align with the crests and troughs of the wave surface elevation, as also observed in the thrust results.

Table 20
The experimental and CFD model results for C_q, C_t and C_p, in wave-current conditions.

Case	C_q			C_t			C_p		
	Exp.	CFD	Dif.	Exp.	CFD	Dif.	Exp.	CFD	Dif.
P1W1	0.123	0.115	0.008	0.909	0.995	0.086	0.470	0.457	0.013
P2W2	0.121	0.119	0.002	0.894	0.990	0.096	0.454	0.460	0.006

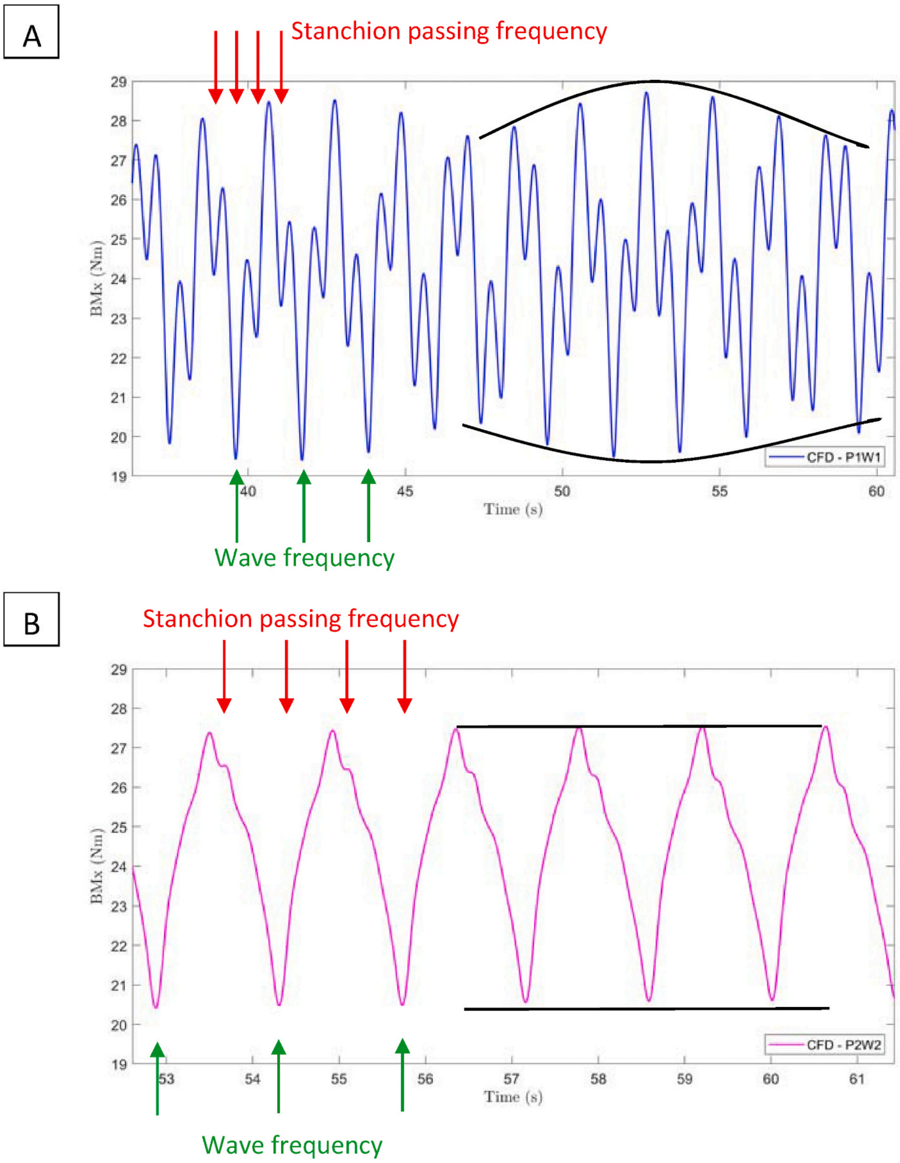

Fig. 23. The CFD results for the out of plane bending moment on a single blade in wave-current conditions representative of A) P1W1; and B) P2W2.

Table 21
The average experimental and CFD BM*x* results for wave-current conditions.

Case	Average out of plane bending moment, BM*x* (Nm)		
	Experimental	CFD	Difference
P1W1	25.85	24.45	1.40
P2W2	25.65	24.58	1.07

These results show the substantial effect that surface waves can have on the loadings of a TST. It is the cyclic nature of the wave induced loadings that can critically affect the fatigue life of the turbine components. Numerical analysis allows researchers and developers to quantify the impact that different flow characteristics can have on marine devices placed in conditions specific to identified tidal test sites.

5. Conclusions

This study presents an experimental test campaign, using a 3-bladed, 1:20 scale, HATT performed at the IFREMER wave-current flume, which is used to validate numerical models under current-only and wave-current conditions. The average and transient turbine thrust, torque and out of plane bending moment were measured both experimentally and numerically, along with the flow velocity and wave height. These measurements allowed the turbine performance characteristics and loads to be calculated. The main conclusions from the study are:

- The turbine was fully characterised under uniform flows, experimentally and numerically, providing a base case of the simplest flow conditions for comparisons against more complex flow investigations.
- The mode of the streamwise velocity was found to accurately represent the predominant flow conditions for all experimental data distributions. When using the mean and the mode in the calculation of the volumetrically averaged streamwise velocity over the swept area of the turbine, differences of up to 4% were found which consequently amplify differences in the calculation of C_q, C_t and C_p of up to 12%.
- Average turbine performance characteristics were unaffected by the presence of a profiled velocity gradient and showed similar results to tests under uniform current conditions.

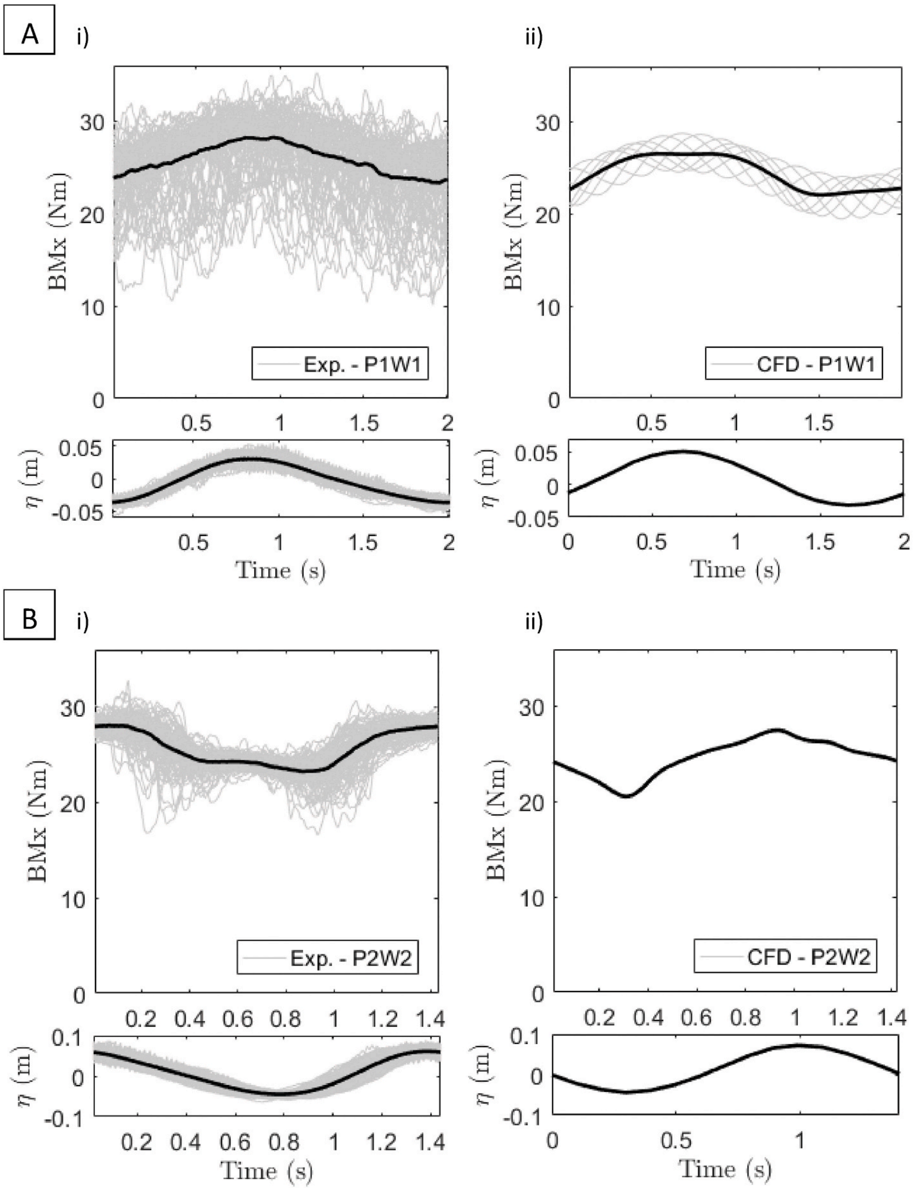

Fig. 24. The average i) experimental and ii) CFD BM*x* fluctuation on a single blade calculated using TSA with the corresponding wave surface elevation for A) P1W1, and B) P2W2 cases.

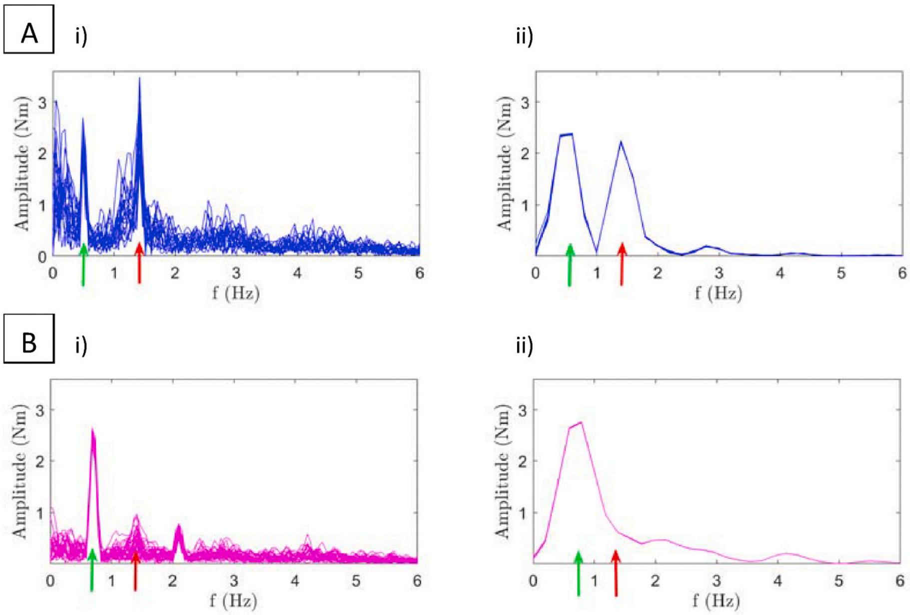

Fig. 25. FFT analysis for the i) experimental and ii) CFD BM*x* results at a TSR of 4 for: A) P1W1 and, B) P2W2 cases. [red arrow = rotational frequency, green arrow = wave frequency].

Table 22
The amplitude of fluctuation in the experimental and CFD BM*x* results.

Case	Amplitude of fluctuation in the BM*x* ± 1 standard deviation, (Nm)					
	Wave frequency			Rotational frequency		
	Experimental	CFD	Difference	Experimental	CFD	Difference
P1W1	2.24 ± 0.24	2.37	0.13	2.56 ± 0.49	2.23	0.33
P2W2	2.50 ± 0.10	2.76	0.26	0.55 ± 0.21	0.62	0.07
U	–	–	–	0.45	0.24	0.21
P1	–	–	–	2.25	2.37	0.12
P2	–	–	–	0.76	0.70	0.06

Table 23
The individual and total turbine thrust and torque loadings when subjected to different flow conditions.

	Average thrust, ***T*** (N)					Average torque, ***Q*** (Nm)				
	U	P1	P2	P1W1	P2W2	U	P1	P2	P1W1	P2W2
Single blade	104.8	102.5	101.7	105.1	107.0	5.6	5.3	5.4	5.6	6.0
Hub	7.9	7.7	7.7	7.9	8.2	0.0	0.0	0.0	0.0	0.0
Total	321.0	314.0	311.7	321.9	327.9	16.6	15.9	16.0	16.8	17.7

- The amplitude of fluctuation in the out of plane bending moment on a turbine blade increased as the shear in the velocity profile intensified, with the highest shearing velocity profile inducing fluctuations 5 times that of the uniform current case. Similar results were found in the turbine blade, thrust and torque results.
- The total thrust and torque loadings showed a reduction in the amplitude of fluctuation due to each turbine blade being 120° out of phase and therefore cancelling out the fluctuation in the loadings.
- The average performance characteristics were unaffected by the inclusion of regular waves.
- Waves induce additional fluctuations in the out of plane bending moment on a single turbine blade; however, the amplitude of these fluctuations is no greater than that caused by the highest shearing velocity profile.
- Cyclic blade loadings are induced by velocity profiles and waves. When analysing the total turbine loadings, only fluctuations induced by wave motion can be observed, with the maximum/minimum loadings being aligned with the crest/trough of the wave, respectively. With the inclusion of waves, the amplitude of fluctuation around the average thrust and torque is 35 times greater that in current-only flows.
- Optimised CFD models were developed to simulate combined wave and current interaction using ANSYS CFX. Uniform and profiled current flows, as well as two regular, intermediate, Stokes 2^{nd} Order Theory wave models were tested and successfully validated using multiple experimental flow and turbine parameters from the IFREMER wave-current flume.
- A set of guidelines were defined which allow any flume geometry and wave characteristic within the Stokes 2^{nd} Order Theory limits to be

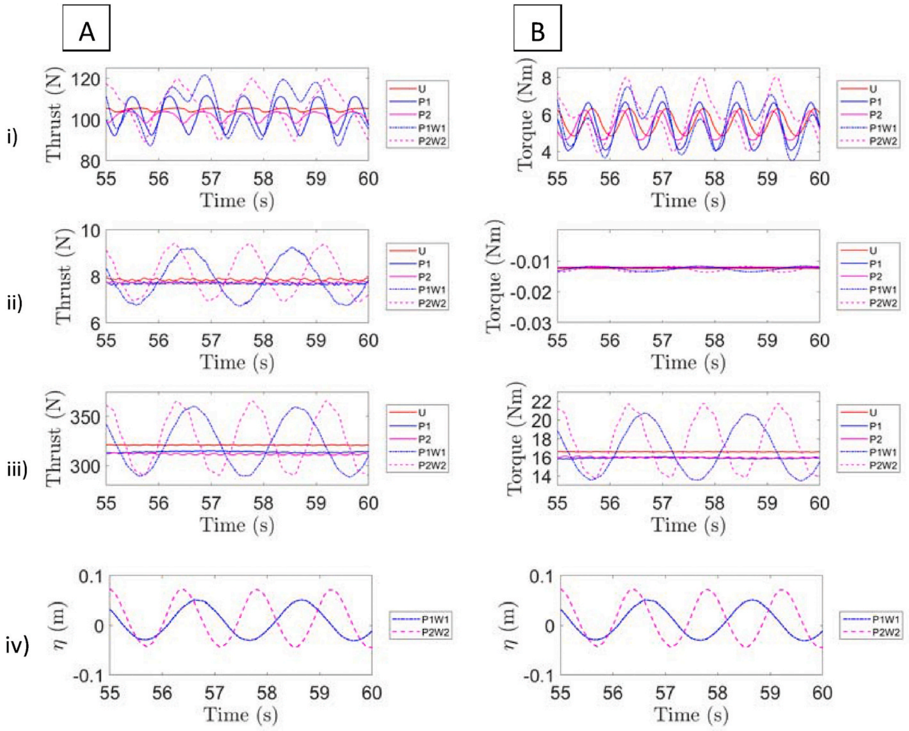

Fig. 26. A CFD comparison for A) thrust and B) torque results at a TSR of 4 relating to: i) a single blade, ii) the hub and; iii) the turbine total (all blades and hub), under current-only (U, P1, P2) and wave-current (P1W1, P2W2) conditions, iv) the surface elevation for W1 and W2 at the turbine location.

Table 24
The fluctuation in the total thrust and torque loadings when subjected to different flow conditions.

	Amplitude of fluctuation in the total thrust, T (N)					Amplitude of fluctuation in the total torque, Q (Nm)				
	U	P1	P2	P1W1	P2W2	U	P1	P2	P1W1	P2W2
Total	0.28	0.19	0.74	33.6	37.8	0.02	0.02	0.07	3.4	3.9

simulated in a free surface model. A HEXA mesh using 120 cells over the length of a wave (Δz) and 10 cells over the wave height (Δy) was found to create a mesh with good numerical accuracy and reasonable computational run time.

These lab-scale results can inform researchers and developers of similar outcomes using full-scale tidal devices. The importance of numerical modelling is also highlighted as its use in the initial stages of device development can reduce the costs associated with device design as well as avoiding the need for a full experimental test campaign and therefore the operational costs of laboratory testing. The wave and current cases used in this study present a controlled set of ocean flow conditions. Further investigation would look to emulate more realistic ocean flow regimes using realistic, high shearing velocity profiles and modelling irregular waves or waves oblique to the current.

CRediT authorship contribution statement

Catherine Lloyd: Conceptualization, Data curation, Formal analysis, Investigation, Methodology, Software, Validation, Writing - original draft. **Matthew Allmark:** Formal analysis, Funding acquisition, Investigation, Methodology, Supervision, Writing - review & editing. **Stephanie Ordonez-Sanchez:** Conceptualization, Investigation, Methodology. **Rodrigo Martinez:** Conceptualization, Investigation, Methodology. **Cameron Johnstone:** Conceptualization, Funding acquisition, Project administration. **Gregory Germain:** Investigation, Writing - review & editing. **Benoit Gaurier:** Investigation, Writing - review & editing. **Allan Mason-Jones:** Conceptualization, Formal analysis, Investigation, Methodology, Supervision, Writing - review & editing. **Tim O'Doherty:** Conceptualization, Funding acquisition, Investigation, Methodology, Project administration, Resources, Supervision, Writing - review & editing.

Declaration of competing interest

The authors declare that they have no known competing financial interests or personal relationships that could have appeared to influence the work reported in this paper.

Acknowledgements

The author acknowledges support from SuperGen UK Centre for Marine Energy [EP/N020782/1] as well as Cardiff University for providing funding. The experimental testing carried out at IFREMER was funded by EPSRC Impact Acceleration Account (IAA) funding [EP/R51150X/1] and the Dynamic Loadings on Tidal Turbine Arrays (DyLoTTA) project [EP/N020782/1]. The author would also like to thank the staff at IFREMER for their expertise and support during the test campaign. In addition, this research was performed using the supercomputing facilities at Cardiff University operated by Advanced Research Computing at Cardiff (ARCCA) on behalf of the Cardiff Supercomputing Facility and the HPC Wales and Supercomputing Wales

(SCW) projects. We acknowledge the support of the latter, which is part-funded by the European Regional Development Fund (ERDF) via the Welsh Government. Information on the data underpinning the results presented here, including how to access them, can be found in the Cardiff University data catalogue at http://doi.org/10.17035/d.2020.0120613428

References

Alberello, A., Pakodzi, C., Nelli, F., Bitner-Gregersen, E.M., Toffoli, A., 2017. Three dimensional velocity field underneath a breaking Rogue wave. In: Proc. ASME 36th Int. Conf. Ocean. Offshore Arct. Eng. June 25-30th 2017, Trondheim, Norw. V03AT02A009. https://doi.org/10.1115/OMAE2017-61237.

Allmark, M., Ellis, R., Lloyd, C., Ordonez-Sanchez, S., Johannesen, K., Byrne, C., Johnstone, C., O'Doherty, T., Mason-Jones, A., 2020. The development, design and characterisation of a scale model horizontal Axis tidal turbine for dynamic load quantification. Renew. Energy.

Allmark, M., Ellis, R., Porter, K., Doherty, T.O., Johnstone, C., 2018. The development and testing of a lab-scale tidal stream turbine for the study of dynamic device loading. In: Proceedings of the 4th Asian Wave and Tidal Energy Conference..

Allmark, M., Grosvenor, R., Prickett, P., 2017. An approach to the characterisation of the performance of a tidal stream turbine. Renew. Energy 111, 849–860. https://doi.org/10.1016/j.renene.2017.05.010.

ANSYS Inc, n.d. ANSYS CFX Modelling Guide.

ANSYS Inc, n.d. ANSYS ICEM.

ANSYS Inc, n.d. ANSYS CFX.

ANSYS Inc, n.d. ANSYS CFX Theory Guide.

ANSYS Inc, n.d. ANSYS CFX Reference Guide.

Bahaj, A.S., Molland, A.F., Chaplin, J.R., Batten, W.M.J., 2007. Power and thrust measurements of marine current turbines under various hydrodynamic flow conditions in a cavitation tunnel and a towing tank. Renew. Energy 32, 407–426. https://doi.org/10.1016/j.renene.2006.01.012.

Bai, X., Avital, E.J., Munjiza, A., Williams, J.J.R., 2014. Numerical simulation of a marine current turbine in free surface flow. Renew. Energy 63, 715–723. https://doi.org/10.1016/j.renene.2013.09.042.

Barltrop, N., Varyani, K.S., Grant, A., Clelland, D., Pham, X.P., 2007. Investigation into wave-current interactions in marine current turbines. In: Proc. IMechE, Part A J. Power Energy, 221, pp. 233–242. https://doi.org/10.1243/09576509JPE315.

Bihs, H., Kamath, A., Chella, A., Aggarwal, A., Arntsen, Ø.A., 2016. A new level set numerical wave tank with improved density interpolation for complex wave hydrodynamics. Comput. Fluids 140, 191–208. https://doi.org/10.1016/j.compfluid.2016.09.012.

Chen, L., Lam, W.H., 2015. A review of survivability and remedial actions of tidal current turbines. Renew. Sustain. Energy Rev. https://doi.org/10.1016/j.rser.2014.11.071.

Ebdon, T., 2019. The Impact of Turbulence and Turbine Operating Condition on the Wakes of Tidal Turbines. PhD Thesis. Cardiff University.

Ellis, R., Allmark, M., O'Doherty, T., Mason-Jones, A., Ordonez-Sanchez, S., Johannesen, K., Johnstone, C., 2018. Design process for a scale horizontal Axis tidal turbine blade. In: Proc. 4th Asian Wave Tidal Energy Conf..

European Commission, 2020a. 2050 long-term strategy | Climate Action [WWW Document]. https://ec.europa.eu/clima/policies/strategies/2050_en. accessed 7.31.20.

European Commission, 2020b. 2030 climate & energy framework | Climate Action [WWW Document]. https://ec.europa.eu/clima/policies/strategies/2030_en#tab-0-0. accessed 7.15.20.

European Commission, 2017. Strategic energy technology plan [WWW Document]. https://doi.org/10.2777/48982.

Finnegan, W., Goggins, J., 2015. Linear irregular wave generation in a numerical wave tank. Appl. Ocean Res. 52, 188–200. https://doi.org/10.1016/j.apor.2015.06.006.

Finnegan, W., Goggins, J., 2012. Numerical simulation of linear water waves and wave-structure interaction. Ocean Eng. 43, 23–31. https://doi.org/10.1016/j.oceaneng.2012.01.002.

Galloway, P.W., Myers, L.E., Bahaj, A.S., 2010. Studies of a scale tidal turbine in close proximity to waves. In: 3rd Int. Conf. Ocean Energy, Bilbao, Spain, 6 Oct 2010 3–8.

Gaurier, B., Davies, P., Deuff, A., Germain, G., 2013. Flume tank characterization of marine current turbine blade behaviour under current and wave loading. Renew. Energy 59, 1–12. https://doi.org/10.1016/j.renene.2013.02.026.

Gaurier, B., Druault, P., Ikhennicheu, M., Germain, G., 2020a. Experimental analysis of the shear flow effect on tidal turbine blade root force from three-dimensional mean flow reconstruction. Phil. Trans. A 378. https://doi.org/10.1098/rsta.2020.0001.

Gaurier, B., Germain, G., Facq, J.V., Johnstone, C.M., Grant, A.D., Day, A.H., Nixon, E., Di Felice, F., Costanzo, M., 2015. Tidal energy "round Robin" tests comparisons between towing tank and circulating tank results. Int. J. Mar. Energy 12, 87–109. https://doi.org/10.1016/j.ijome.2015.05.005.

Gaurier, B., Grégory, G., Jean-Valéry, F., Thomas, B., 2018. WAVE and CURRENT FLUME TANK of BOULOGNE-SUR-MER Description of the Facility and its Equipment.

Gaurier, B., Ordonez-Sanchez, S., Facq, J., Germain, G., Johnstone, C., Martinez, R., Salvatore, F., Santic, I., Davey, T., Old, C., Sellar, B., 2020b. MaRINET2 tidal energy round robin tests-performance comparison of a horizontal axis turbine subjected to combined wave and current conditions. J. Mar. Sci. Eng. 8 https://doi.org/10.3390/JMSE8060463.

Hafeez, N., Badshah, S., Badshah, M., Khalil, Sakhi Jab, 2019. Effect of velocity shear on the performance and structural response of a small-scale horizontal axis tidal turbine. Mar. Syst. Ocean Technol. https://doi.org/10.1007/s40868-019-00057-0.

Henriques, T.A., Tedds, S.C., Botsari, A., Najafian, G., Hedges, T.S., Sutcliffe, C.J., Owen, I., Poole, R.J., 2014. The effects of wave-current interaction on the performance of a model horizontal axis tidal turbine. Int. J. Mar. Energy 8, 17–35. https://doi.org/10.1016/j.ijome.2014.10.002.

Henriques, T., Hedges, T., Owen, I., Poole, R., 2016. The influence of blade pitch angle on the performance of a model horizontal axis tidal stream turbine operating under wave-current interaction. Energy 102. https://doi.org/10.1016/j.energy.2016.02.066.

Holst, M., Gunnar Dahlhaug, O., Faudot, C., 2015. CFD analysis of wave-induced loads on tidal turbine blades. IEEE J. Ocean. Eng. 40.

Howell, R., Qin, N., Edwards, J., Durrani, N., 2009. Wind tunnel and numerical study of a small vertical axis wind turbine. Renew. Energy 35, 412–422. https://doi.org/10.1016/j.renene.2009.07.025.

Jacobsen, N., Fuhrman, D., Fredsøe, J., 2012. A wave generation toolbox for the open-source CFD library: OpenFoam. Int. J. Numer. Methods Fluid. 70, 1073–1088. https://doi.org/10.1002/fld.2726.

Lal, A., Elangovan, M., 2008. CFD simulation and validation of flap type wave-maker. Int. J. Math. Comput. Sci. 2, 708–714.

Lambert, R., 2012. Development of a Numerical Wave Tank Using OpenFOAM. PhD Thesis. University of Coimbra.

Li, X., Li, M., Jordan, L.-B., McLelland, S., Parsons, D.R., Amoudry, L.O., Song, Q., Comerford, L., 2019. Modelling impacts of tidal stream turbines on surface waves. Renew. Energy 130, 725–734. https://doi.org/10.1016/j.renene.2018.05.098.

Liang, X.-F., Yang, J.-M., Li, J., Long-Fei, X., Xin, L., 2010. Numerical simulation of irregular wave - simulating irregular wave train. J. Hydrodyn. 22, 537–545. https://doi.org/10.1016/S1001-6058(09)60086-X.

Lloyd, C., 2020. The Performance of a Tidal Stream Turbine under Wave and Current Interaction. PhD Thesis. Cardiff University.

Lloyd, C., Allmark, M., Ellis, R., Ordonez-Sanchez, S., Mason-Jones, A., O'Doherty, T., Germain, G., Gaurier, B., 2019a. CFD surface effects on flow conditions and tidal stream turbine performance. In: Proceedings of the 13th European Wave and Tidal Energy Conference.

Lloyd, C., O'Doherty, T., Mason-Jones, A., 2019b. Development of a wave-current numerical model using Stokes 2nd Order Theory. Int. Mar. Energy J. 2, 1–14. https://doi.org/10.36688/imej.2.1-14.

Lust, E., Luznik, L., Flack, K., Walker, J., Van Benthem, M., 2013. The influence of surface gravity waves on marine current turbine performance. Int. J. Mar. Energy 3–4, 27–40.

Luznik, L., Flack, K.A., Lust, E.E., Taylor, K., 2013. The effect of surface waves on the performance characteristics of a model tidal turbine. Renew. Energy 58, 108–114. https://doi.org/10.1016/j.renene.2013.02.022.

Maganga, F., Germain, G., King, J., Pinon, G., Rivoalen, E., 2010. Experimental characterisation of flow effects on marine current turbine behaviour and on its wake properties. IET Renew. Power Gener. 4 https://doi.org/10.1049/iet-rpg.2009.0205.

Mani, J.S., 2012. Coastal Hydrodynamics. PHI Learning Private Limited, New Delhi.

Marques Machado, F.M., Gameiro Lopes, A.M., Ferreira, A.D., 2018. Numerical simulation of regular waves: optimization of a numerical wave tank. Ocean Eng. 170, 89–99. https://doi.org/10.1016/j.oceaneng.2018.10.002.

Martinez, R., Ordonez-Sanchez, S., Allmark, M., Lloyd, C., O'Doherty, T., Germain, G., Gaurier, B., Johnstone, C., 2020. Analysis of the effects of control strategies and wave climates on the loading and performance of a laboratory scale horizontal axis tidal turbine. Ocean Eng. 212 https://doi.org/10.1016/j.oceaneng.2020.107713.

Mason-Jones, A., 2010. Performance Assessment of a Horizontal Axis Tidal Turbine in a High Velocity Shear Environment. PhD Thesis. Cardiff University.

Mason-Jones, A., O'Doherty, D.M., Morris, C.E., O'Doherty, T., 2013. Influence of a velocity profile & support structure on tidal stream turbine performance. Renew. Energy 52, 23–30. https://doi.org/10.1016/j.renene.2012.10.022.

McSherry, R., Grimwade, J., Jones, I., Mathias, S., Wells, A., Mateus, A., 2011. 3D CFD modelling of tidal turbine performance with validation against laboratory experiments. In: Proc. 9th EWTEC Southampton, UK.

Menter, F.R., 1996. A comparison of some recent eddy-viscosity turbulence models. J. Fluid Eng. 118, 514–519.

O'Doherty, T., Mason-Jones, A., O'Doherty, D.M., Byrne, C.B., Owen, I., Wang, Y.X., 2009. Experimental and computational analysis of a model horizontal Axis tidal turbine. In: Proceedings of the 8th European Wave and Tidal Energy Conference, Uppsala, Sweden. Uppsala, Sweden, pp. 833–841.

O'Doherty, T., Mason-Jones, A., O, D.M., Evans, P.S., Wooldridge, C., Fryett, I., 2010. Considerations of a horizontal axis tidal turbine. Energy 163. https://doi.org/10.1680/ener.2010.163.3.119.

Ocean Energy Europe, 2018. Ocean Energy: Key Trends and Statistics 2018 [WWW Document]. http://www.oceanenergy-europe.eu/wp-content/uploads/2019/04/Ocean-Energy-Europe-Key-trends-and-statistics-2018_web.pdf.

Ordonez-Sanchez, S., Allmark, M., Porter, K., Ellis, R., Lloyd, C., Santic, I., O'Doherty, T., Johnstone, C., 2019. Analysis of a horizontal-Axis tidal turbine performance in the presence of regular and irregular waves using two control strategies. Energies 12, 367. https://doi.org/10.3390/en12030367.

Ordonez-Sanchez, S., Porter, K., Frost, C., Allmark, M., Johnstone, C., 2016. Effects of wave-current interactions on the performance of tidal stream turbines. In: Narasimalu, S. (Ed.), Proceedings of the 3rd Asian Wave & Tidal Energy Conference. Research Publishing, Singapore, pp. 394–403.

Porter, K., Ordonez-Sanchez, S., Murray, R., Allmark, M., Johnstone, C., O'Doherty, T., Mason-Jones, A., Doman, D., Pegg, M., 2020. Flume testing of passively adaptive composite tidal turbine blades under combined wave and current loading. J. Fluid Struct.

Raval, A., 2008. Numerical Simulation of Water Waves Using Navier-Stokes Equations. PhD Thesis. University of Leeds.

Renewable Energy Association, 2019. Marine - renewable technologies [WWW Document]. Inf. Mar. https://www.r-e-a.net/renewable-technologies/marine. accessed 10.18.19.

Sorensen, R., 2006. Basic Coastal Engineering, third ed. John Wiley & Sons, Pensylvania.

Sos, M., Johnston, L., Walker, J., Rahimian, M., 2017. The impact of waves and immersion depth on HATT performance. In: Proc. 12th Eur. Wave Tidal Energy Conf. 27th Aug -1st Sept 2017, Cork, Irel. 1–8.

Sun, X., Chick, J.P., Bryden, I.G., 2008. Laboratory-scale simulation of energy extraction from tidal currents. Renew. Energy 33, 1267–1274. https://doi.org/10.1016/j.renene.2007.06.018.

Tatum, S.C., Frost, C.H., Allmark, M., O'Doherty, D.M., Mason-Jones, A., Prickett, P.W., Grosvenor, R.I., Byrne, C.B., O'Doherty, T., 2016. Wave-current interaction effects on tidal stream turbine performance and loading characteristics. Int. J. Mar. Energy 14, 161–179. https://doi.org/10.1016/j.ijome.2015.09.002.

Tian, X., Wang, Q., Liu, G., Deng, W., Gao, Z., 2018. Numerical and experimental studies on a three-dimensional numerical wave tank. IEEE Access. https://doi.org/10.1109/ACCESS.2018.2794064.

Togneri, M., Masters, I., 2016. Micrositing variability and mean flow scaling for marine turbulence in Ramsey Sound. J. Ocean Eng. Mar. Energy 2, 35–46. https://doi.org/10.1007/s40722-015-0036-0.

U.S Energy Information Administration, 2017. International Energy Outlook 2017 [WWW Document]. www.eia.gov/ieo. accessed 12.13.17.

UK Department for Business Energy and Industrial Strategy, 2020. Section 5 - UK Electricity January to March 2020.

Yan, J., Deng, X., Korobenko, A., Bazilevs, Y., 2017. Free-surface flow modeling and simulation of horizontal-axis tidal-stream turbines. Comput. Fluids 158, 157–166. https://doi.org/10.1016/j.compfluid.2016.06.016.